

Arredondo, R., Oberkofler, M., Schmid, K., Schwarz-Selinger, T.,  
Seidl, L., Jacob, W., Neu, R.

## **SIESTA: a High Current Ion Source for Erosion and Retention Studies**

**IPP 2018-21  
Oktober 2018**

# SIESTA: a High Current Ion Source for Erosion and Retention Studies

R. Arredondo<sup>1,2\*</sup>, M. Oberkofler<sup>1</sup>, K. Schmid<sup>1</sup>,  
T. Schwarz-Selinger<sup>1</sup>, L. Seidl<sup>2</sup>, W. Jacob<sup>1</sup>, R. Neu<sup>1,2</sup>

<sup>1</sup>*Max Planck Institut für Plasmaphysik, Garching, Germany*

<sup>2</sup>*Technische Universität München, Garching, Germany*

\**rodrigo.arredondo@ipp.mpg.de*

## Abstract

SIESTA (Second Ion Experiment for Sputtering and TDS Analysis) is a high-current ion source for erosion and retention studies with focus on wall materials for fusion devices. The system is composed of a DuoPIGatron type ion source, three consecutive grids for ion extraction as well as acceleration and beam focusing, a differential pumping stage, a dipole magnet for mass filtering, a quadrupole doublet lens, a target chamber, a load-lock and a chamber for thermal desorption spectrometry. The potential of the source can be varied between 200 V and 10 kV. The target chamber has a base pressure of  $10^{-8}$  mbar, and an operating pressure of  $10^{-7} - 10^{-6}$  mbar. The target can be rotated to study angle-dependent effects, heated via electron-impact heating up to 1300 K for high temperature erosion and implantation studies. The target chamber is equipped with an in-situ magnetic suspension balance. The operating parameters of the ion source were mapped to achieve the maximum ion current at the target for various gas species and accelerating potentials. The beam emittance for a  $D_3^+$  ion beam was measured after deflection in the dipole magnet. This was used for ion beam simulations, which aided the design of the quadrupole lenses. If the quadrupole doublet is used, the ion flux to the target is increased by up to a factor of 4. Additionally, the relative population of neutral particles present in the beam at the target was quantified. The typical beam footprint at the target under normal incidence has an area of  $0.5 \text{ cm}^2$ . The ion current reaching the target increases with the accelerating potential. Due to this effect, the ion flux density at the target in the low-ion-impact-energy range can be increased by operating the source at a higher extraction potential and by applying a (decelerating) potential to the target, rather than directly operating the ion source at a lower potential. Ion impact energies as low as  $200 \text{ eV/D}$  are achieved this way with a  $D_3^+$  current of  $100 \mu\text{A}$  when focusing the beam with the quadrupole doublet lens, equating to an ion flux density of  $3.7 \times 10^{19} \text{ m}^{-2}\text{s}^{-1}$  with a beam footprint of approximately  $0.5 \text{ cm}^2$ . At ion impact energies of  $2 \text{ keV/D}$ , the maximum achievable flux density with  $D_3^+$  is  $6 \times 10^{19} \text{ m}^{-2}\text{s}^{-1}$ . Experimental determination of sputter yields was performed via in-vacuo and ex-situ weight loss measurement for bulk Au samples, showing reasonably good agreement with simulations and experimental data from literature.

## Foreword

This IPP report constitutes an extended version of the article published under the same title by the authors. This version is included in the Supplementary Material of said article, and includes more detailed descriptions of technical details and beam characterizations [1].

## 1 Introduction

The choice of plasma-facing material is highly significant for future fusion devices, as it imposes a series of safety, operational and economic constraints on the device. In particular, three issues have been identified as critical: the lifetime of plasma-facing components (PFCs), dust production from the erosion of PFCs and tritium retention in the inner walls of the device [2].

In the case of the first wall, erosion is caused predominantly by an intense flux of neutral particles, which are neutralized close to the plasma edge and are, therefore, no longer confined by the magnetic field. This neutral particle flux density is estimated to be in the range of  $10^{19} - 10^{21} \text{ m}^{-2}\text{s}^{-1}$ , with impinging particle energies normally in the  $8 - 300 \text{ eV}$  range [2]. In this energy range, erosion is driven by physical sputtering [3], and can be accurately simulated by Coulomb interactions [4]. This process can also be studied experimentally, either in plasma devices which emulate the conditions of the plasma edge of a fusion reactor, or with the use of an ion source. Plasma devices allow for high particle flux densities to the target surface in the desired particle energy range. However, the presence of impurities, multiple ion species and a not easily determinable flux of energetic neutrals along with the intrinsic energy spread of the particles can make the quantitative analysis of results difficult. In contrast, ion sources have a number of distinct advantages over plasma devices, producing a mono-energetic beam which can be mass-filtered with magnetic sector fields, allowing for well-defined experiments. Historically, these machines have achieved significantly lower particle flux densities than their plasma counterparts, leading to longer exposure times to reach the desired fluence.

SIESTA (Second Ion Experiment for Sputtering and TDS Analysis) helps to bridge this gap, aiming to provide higher particle flux densities without losing the advantages of the ion source setup. SIESTA is the successor of the pre-existing HSQ (in German, *HochStrom.Quelle*) [5], which during its over 40 years of operation at the Max Planck Institute of Plasma Physics in Garching was instrumental in over 200 publications. At SIESTA, a DuoPIGatron type ion source is employed to provide particle flux densities of several  $10^{19} \text{ m}^{-2}\text{s}^{-1}$  to the target with a mono-energetic, mass-filtered ion beam (typically  $D_3^+$ ), with a final operating energy range of  $200 \text{ eV} - 10 \text{ keV}$ . The device is described in detail in section 2, and section 3 details the results of the characterization of SIESTA. The sputter yield of Au by deuterium atoms with an impact energy of  $2 \text{ keV}$  was measured and contrasted with simulations and other experimental data, shown in section 4. Finally, the main conclusions are summarized in section 5.

## 2 Description of the experimental setup

### 2.1 Overview

A principle overview of the individual components of SIESTA is presented in this section. Fig. 1 shows a bird's eye view of SIESTA along with its main elements. The most important components are described in more detail in the following sections.

A plasma is generated inside the ion source, which is set to a high (positive) potential of maximum  $10 \text{ kV}$ , which determines the extracted ion energy. A series of three grids, the first at ion source potential and the last at ground potential, separate the ion source from the rest of the beam path. The ions that diffuse towards the grids are accelerated by the potential difference in the space between them, leading to a stationary ion beam of the desired energy. The intermediate grid serves to repel electrons away from the positively-biased ion source and is described in more detail in section 2.2.

The neutral gas from the ion source is mostly pumped in the differential pumping stage. The beam diameter is limited at the exit of the differential pumping stage by a  $\text{Ø } 16 \text{ mm}$  Mo aperture (fig. 2). A pneumatically-actuated beam-stopper, described in more detail in section 2.4, is located directly behind this aperture.

Behind the Mo aperture and with the beam stopper retracted, the beam passes through the dipole magnet. Each ion species present in the beam is deflected, with a radius of curvature proportional to the square root of its mass, thereby splitting the beam (discussed in further detail in section 2.5). The magnetic field is varied to allow only the desired ion species to exit through the opening to the target chamber, situated at a  $44^\circ$  angle from the dipole magnet entrance.

The target is housed in a double cage that serves as an electrical screening element and as a secondary electron catcher for the ion current measurement at the target. On its trajectory, the beam is cropped by an adjustable aperture into a circular or elongated shape and passes through openings in the double cage before impinging on the target.

The target can be rotated and heated via electron-impact heating. Further it can be set to a positive potential in order to decelerate incoming ions and thus study erosion at low (i.e., sub-keV) particle energies while continuing to operate the ion source at a high accelerating potential, which produces high particle flux densities. A magnetic suspension balance enables in-situ weight loss measurement of the sample.

Samples can be loaded via a lateral, separately-pumped load-lock with a horizontal manipulator. A vertical manipulator at the load-lock can be used to transfer the sample to the Thermal Desorption Spectroscopy (TDS) chamber, located directly underneath. This enables in-vacuo TDS measurements of, e.g., released hydrogen isotopes directly after implantation.

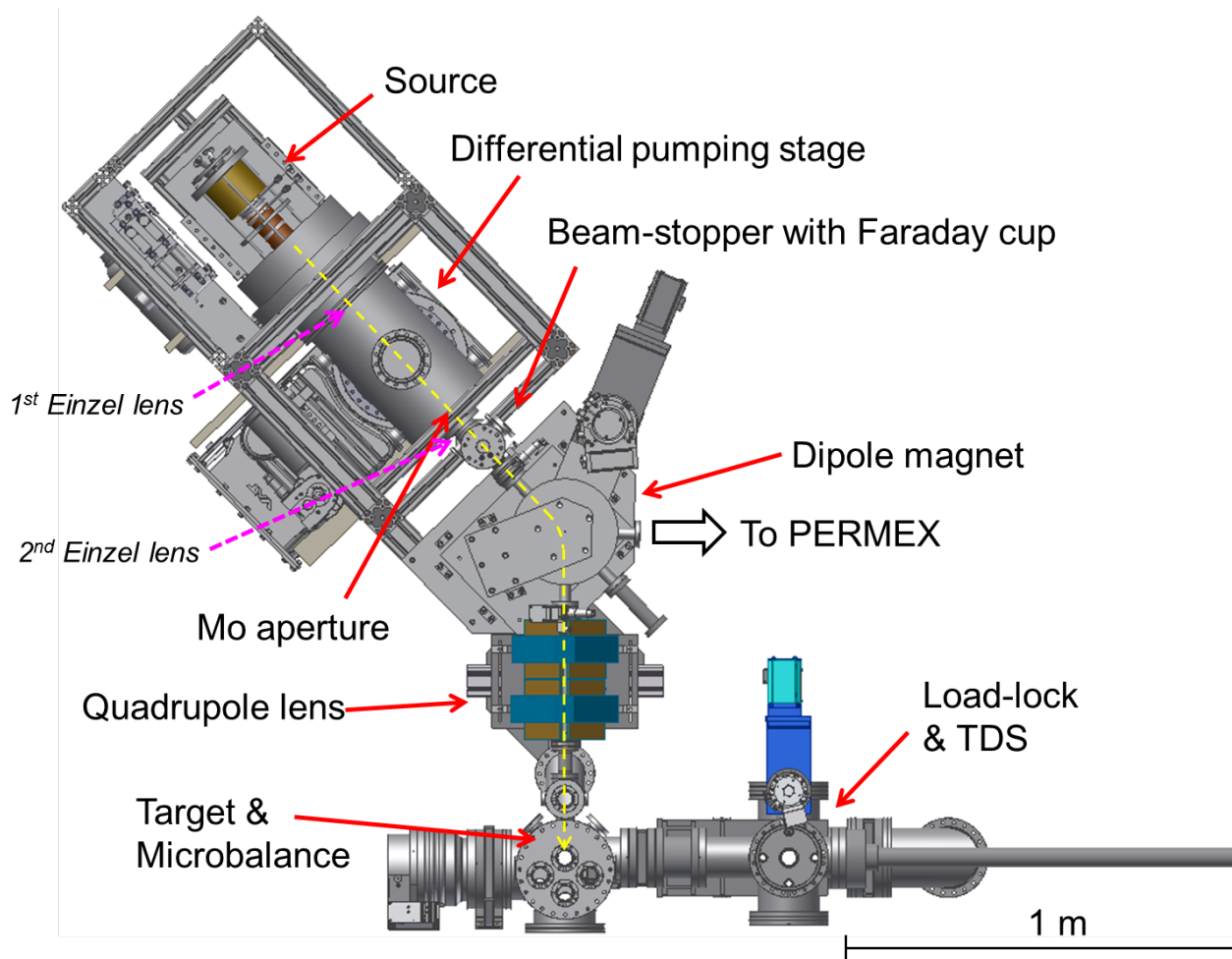


Figure 1: CAD bird's-eye view of SIESTA. The yellow dashed arrow indicates the ion trajectory from the ion source to the target. The einzel lenses (marked with dashed magenta arrows) were later removed and are described in more detail in section 3.3. The new version of the ion-driven permeation experiment PERMEX will be located at the exit of the dipole magnet labeled "To PERMEX" .

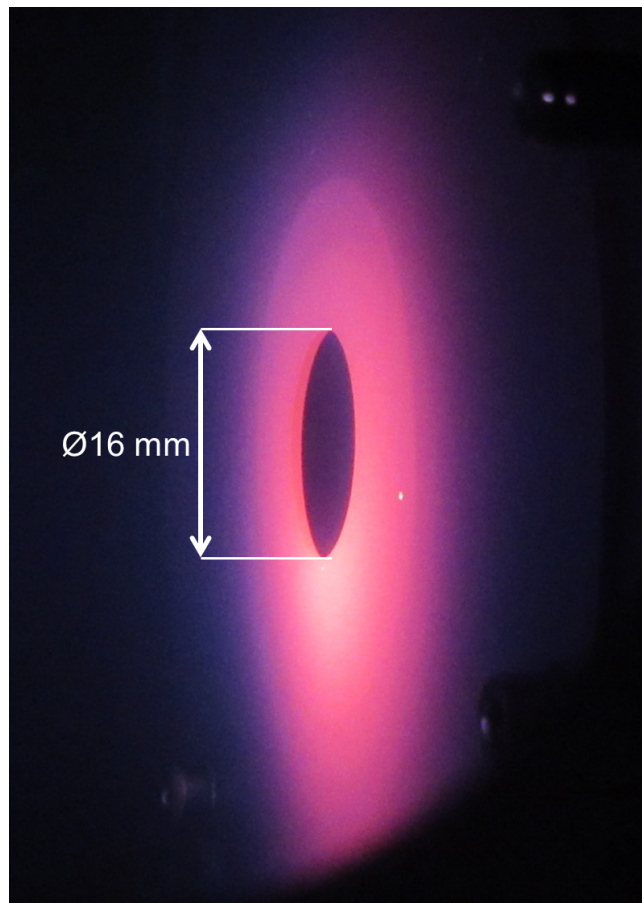


Figure 2: Deuterium ion beam impinging on the Mo aperture located at the end of the first differential pumping stage, as seen from the side facing the ion source through a lateral viewing port. Despite active water cooling, the heat load from the ion beam is sufficient to heat the aperture to temperatures at which it begins to glow. Given the layout of the cooling circuit, cooling efficiency is lower directly below the aperture, leading to higher temperatures in this region and causing it to shine brighter. The purple haze surrounding the aperture is due to recombination light emitted when the impinging D ions neutralize. The aperture is fixed to the differential pumping stage by hex screws situated around the aperture. One such screw is visible on the lower left side of the image.

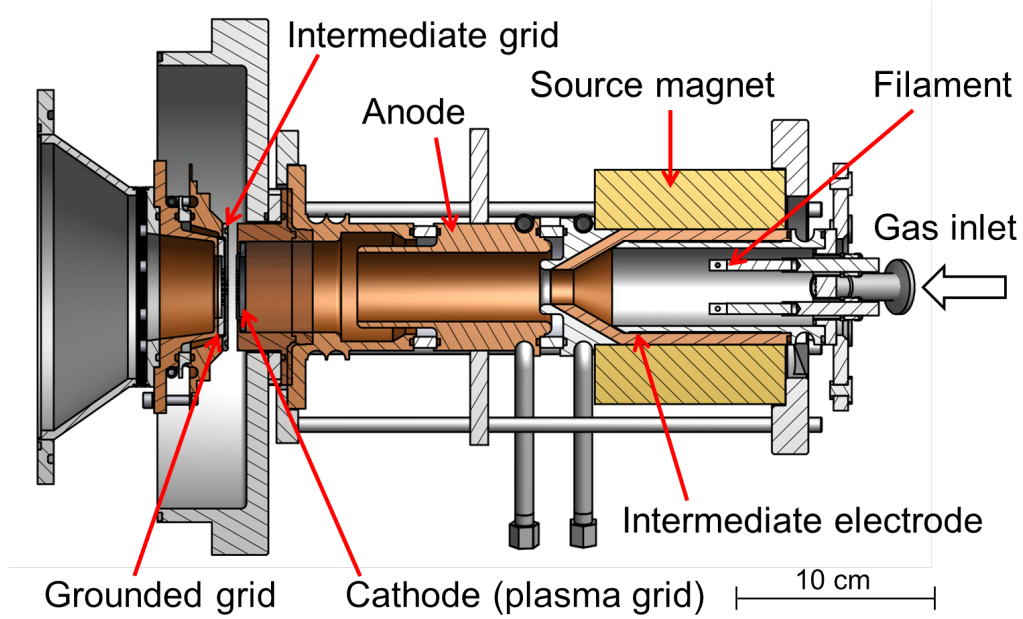


Figure 3: Half-section view of the DuoPIGatron ion source. No filament is in place in the figure.

## 2.2 DuoPIGatron ion source, gas supply & cooling system

The DuoPIGatron ion source was developed by Davis et al. as a variation of the pre-existing 4-electrode duoplasmatron device, consisting of a Penning Ion Gauge (PIG) discharge with a plasma feed from the duoplasmatron source [6]. It was designed to serve as a high-current positive ion source for continuous or pulsed operation, and was used as main ion source for plasma heating via neutral beam injection [6, 7].

The coated filament in the ion source is heated to produce electrons through thermionic emission. A potential difference of 40 V is used to accelerate the electrons to the cylindrical anode (shown in fig. 3), forming a stable arc typically set to an arc current of 12 A. As gas is let in through the chamber, a low-pressure gas discharge is formed and compressed to a high ionization degree in the ferromagnetic intermediate electrode, surrounded by an electromagnet. The ions exiting the intermediate electrode are confined in a PIG discharge, with the intermediate electrode acting as first cathode. It is separated from the plasma grid (taking the role of the complementary cathode) by the hollow anode. The plasma expands radially near the plasma grid, also known as extraction grid in the literature, and a radially homogeneous beam is observed at the plasma grid [7]. The source floats at the extraction voltage, which can be set up to 10 kV, as do the flow controllers for the gas inlet. Beyond the plasma grid, two more grids are present: an intermediate grid set to a low negative potential of up to -165 V and a final grounded grid. Ions are accelerated out of the source in the 3.7 mm gap between the first (extraction) and second (intermediate) grid. This intermediate grid serves to repel electrons emitted in beam charge exchange reactions in the first differential pumping stage that would otherwise be accelerated towards the ion source. These electrons facilitate high space charge compensation in the beam. The spacing between intermediate and grounded grid is 0.7 mm. The physical limit to the current that can be extracted from the ion source is given by the Child-Langmuir law [8]:

$$I = \frac{4\pi\epsilon_0}{9} \sqrt{\frac{2e}{m}} \left(\frac{a}{d}\right)^2 U^{3/2}, \quad (1)$$

where  $I$  is the maximum current that can be extracted from an ion source aperture with radius  $a$ , with  $U$  the extraction potential and  $d$  the space between the extraction and grounded (or in this case intermediate) grids.  $\epsilon_0$  corresponds to the vacuum permittivity,  $m$  is the mass of the extracted ions and  $e$  is the elementary charge. It can be deduced from equation 1 that high extraction potentials and a grid spacing as small as technically possible while avoiding breakdown are desired.

In practice, perveance is defined as [9]:

$$\Pi = \frac{I}{U^{3/2}}. \quad (2)$$

Which only if operating an ion source in a space-charge-limited regime takes the form of:

$$\Pi_{max} = \frac{4\pi\epsilon_0}{9} \sqrt{\frac{2e}{m}} \left(\frac{a}{d}\right)^2. \quad (3)$$

The electric field in the gap between grids also has the effect of focusing the beam, thereby affecting the beam divergence at the exit of the ion source. This focusing effect is dependent on the plasma parameters,



Figure 4: High-voltage cage of the DuoPIGatron ion source. Below the source, the cooling lines coiled into double spirals can be observed.

as these can affect the shape of the plasma meniscus, the equipotential surface at the extraction grid aperture that serves as an artificial boundary between the field-free plasma and the extraction region. There exists a perveance optimum  $\Pi_{opt} < \Pi_{max}$  at which beam divergence is minimal [9, 10]. In practice, since high ion currents are typically desired at the target and not at the exit of the ion source, sources like the DuoPIGatron are often operated closer to the optimal rather than the maximum perveance to benefit from the decreased beam divergence [9].

The source is located within an aluminum high-voltage cage made from item MB Building Kit System<sup>1</sup> standard parts, PEEK (PolyEther Ether Ketone, a thermoplastic polymer) and PMMA (Polymethyl methacrylate, acrylic glass), as seen in fig. 4. The door to the cage is connected to an interlock which shuts off the ion source power supplies in the event of the door being opened.

The filament is composed of a tantalum wire, chosen for its high melting point, coated with a mixture of low-work-function compounds, which facilitate good thermionic emission at relatively low filament temperatures. Before coating, the filament is wrapped in a nickel mesh to increase the wettability surface for the coating to the filament. The coating is a mixture of nickel, barium carbonate and strontium carbonate, at a proportion of 8:1:1 in volume, respectively. Originally in powder form, the solid coating mixture is dissolved in pure analysis-grade ethanol and is applied to the filament with a brush, at which point it is allowed to dry for some 1-2 minutes before applying another layer of coating. 2-3 layers are usually required to achieve a sufficiently thick coating. After this step, the filament can be mounted on the vacuum flange housing the gas inlet and the electrical feed-throughs. Fig. 5 shows the coiled filament before coating, along with an uncoiled filament and the brass cylinder in the background.

All three grids present the same configuration, consisting of 37  $\varnothing$  2 mm holes with 1 mm spacing with an effective diameter of  $\varnothing$  20 mm organized hexagonally for high transparency (up to 60%). As a consequence of this design choice, the grids are only cooled around their respective edges, and so are not optimized to withstand high heat loads [7]. This limits the extraction voltage of the source and consequently the total extractable ion current, especially in steady state operation. The grids were manufactured from TZM, a 99 % molybdenum alloy with better mechanical and manufacturing properties than pure molybdenum, yet still retaining the advantages of high melting point and very low coefficient of thermal expansion [11]. Molybdenum screws were used to secure the first grid to the copper cooling ring, as it was seen that stainless steel screws lead to partial melting and fracture from thermal stress, due to the two materials' different thermal expansion coefficients, as seen in

<sup>1</sup>Registered trademark of item Industrietechnik GmbH



Figure 5: Coiled ion source filament before coating. In the background, the grooved brass cylinder used to coil the filament and an uncoiled tantalum filament, already wrapped in a nickel mesh, can be seen.

fig. 6. To maximize the beam transmission, the three grids were aligned hole-on-hole and all three were aligned co-axially with the rest of the ion source with stiff  $\varnothing$  2 mm rods of an adequate tolerance and optically via an adjustable precision telescope.

The gas supply consists of up to four 2-liter pressurized gas bottles, each connected to a pressure regulator with a maximum pressure rating of 300 bar and a maximum output rating of 10 bar. Each line has its own bypass leading to a common venting line which can be evacuated with a Kashiyama NeoDry 15E<sup>2</sup> dry vacuum pump. After the venting line bypass, the first and second lines are connected together, as are the third and fourth lines. Each line is then introduced into the high voltage cage via a ceramic insulator, as shown in fig. 7 (labeled “To source”). To avoid a gas discharge within the ceramic insulator, the pressure in the lines must during operation be maintained at a value above the one dictated by the Paschen curve for the selected gas species [12]. This is assured with switch manometers in the gas lines connected to the ion-source interlock. At a pressure below 3 bar, the switches are open and it is impossible to operate the ion source. Stainless steel tubes with an outer diameter of 6 mm are used for the complete gas supply system. All connections are made with Swagelok<sup>3</sup> components.

The gas flow is controlled by two Bronkhorst EL-FLOW<sup>4</sup> electronic flow controllers within the high voltage cage, allowing a maximum flow rate of 20 sccm (standard cubic centimeters per minute). A typical flow rate when using deuterium is 10 sccm. The flow controllers are operating at source potential and are powered through a galvanically separated transformer. They are controlled through proprietary Bronkhorst<sup>5</sup> software via an RS232 connection. Fiber-optic waveguides with RS232-frequency couplers are used to maintain the galvanic separation between computer and flow controllers.

Deuterium was used to characterize the ion source. Hydrogen, helium and argon have also been tested. However, when producing argon or helium plasma, the source must first be ignited with hydrogen, and then the hydrogen flow must be partially reduced in favor of the desired gas.

A series of FUG<sup>6</sup> power supplies are used to provide power to the ion source and to set it to the desired

<sup>2</sup>Trademark of Kashiyama Industries, Ltd.

<sup>3</sup>Registered trademark

<sup>4</sup>Trademark of BRONKHORST HIGH-TECH B.V.

<sup>5</sup>Trademark of Bronkhorst High-Tech B.V.

<sup>6</sup>Trademark of FuG Elektronik GmbH



Figure 6: Ion source extraction grid with partly-melted steel screws. The screw heads have either melted or have broken off due to thermal stresses.

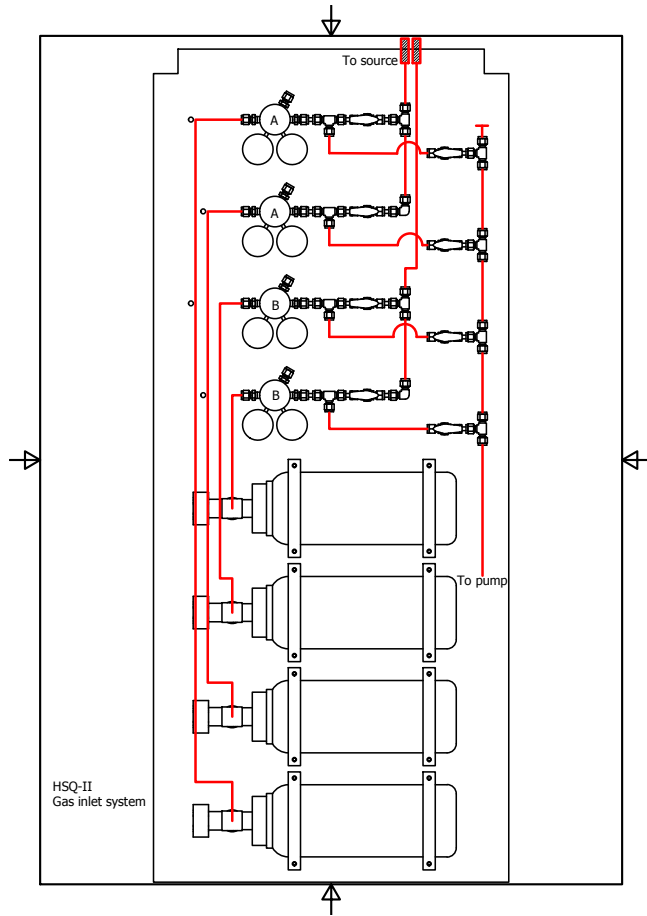


Figure 7: Draft of the gas connection scheme of SIESTA.

accelerating potential. All power supplies are insulated up to 15 kV and are grounded relative to the extraction grid potential. The connection scheme of the source components is detailed in fig. 8. Typical values are listed in table 1.

To prevent overheating, three separate cooling lines are used to cool the ion source, ion source magnet, dipole magnet, beam stopper, ion source grids and Mo aperture. All ion source components, with the exception of the source magnet shown in fig. 3 (i.e. filament, intermediate electrode, anode and cathode), are cooled by a dedicated cooling circuit with a de-mineralized water-water heat exchanger. (FCUN004 model from National Lab<sup>7</sup>) at a nominal pumping pressure of 2.9 bar. The source magnet is made of a coiled rectangular copper tube with channel dimensions of 1 x 2 mm, outer section of 3x4 mm and an uncoiled length of several meters, insulated with cellulose and resin. As a consequence of this design, the cooling water through the source magnet is subject to large pressure losses. For this reason, a separate cooling circuit with an air-water heat exchanger and pump delivering a nominal pressure of 3 bar (PCNO 10 from National Lab) is used for the source magnet. De-mineralized water is used to prevent current losses through these two cooling circuits between the ion source and the cooling water pumps and heat exchangers. The water conductivity is measured periodically. The cooling lines of both of these circuits are coiled into two sets of concentric spirals below the source, one for the inlet line and the other for the outlet, in order to increase the effective length of the cooling lines before exiting the housing cage of the source, helping to reduce current losses through the water lines. The coiled cooling lines are shown in fig. 4. The second (intermediate) and third (grounded) grids are cooled separately with a third cooling circuit, which also supplies water to the Mo aperture, beam-stopper and dipole magnet, consisting of a water-water heat exchanger and pump (FCUN001 from National Lab). Since these components are either grounded or set to low voltages (under 200V), no de-mineralized water is required in this cooling circuit. The secondary circuits of the two water-water heat exchangers are supplied with cooling water from the building at a constant temperature of 14°C. A pressure regulator is installed before the inlet of the secondary circuits, lowering the inlet pressure from 6 bar to 3 bar. A solenoid valve installed after the pressure regulator is connected to two water sensors placed on the floor. In case of a water leak, the sensors will open the electric circuit powering the solenoid valve, which will close, stopping the flow of water. Flow meters are installed in each primary and secondary cooling line. If the water flow in any of these lines is lower than a pre-defined value, the ion source is switched off to prevent over-heating of the source components.

Power supply	Voltage [V]	Current [A]
High Voltage	6000	0.028
Filament	4.2	20
Magnet	5.8	20
Arc	195	12

Table 1: Typical currents and voltages applied by the ion source power supplies when using deuterium.

## 2.3 Vacuum system

SIESTA can be divided into five separate high-vacuum chambers: The ion source and differential pumping stage including beam-stopper, the dipole magnet, the target chamber including quadrupole lenses and antechamber, the load-lock and the TDS chamber. Each chamber is separated from its neighbors by a high-vacuum gate valve and is outfitted with its own turbomolecular pump, which is also separated from the vacuum chamber by another gate valve. Each turbomolecular pump is connected to one of two rotary vane vacuum pumps. Operationally, these two rough vacuum pumps mean that SIESTA comprises two entirely separate vacuum systems: a “clean” vacuum system for the target chamber and TDS chamber, and a “general” system for the rest of the components. Additionally, the aforementioned dry vacuum pump for pumping of the gas inlet system (see Sect. 2.2) is used as a bypass pump and is connected to each turbomolecular pump and to the load-lock. This allows for each vacuum chamber and turbomolecular pump to be either pumped or vented independently of the rest, which is useful for maintenance operations. A schematic of the vacuum system is shown in fig. 9.

The rotary vane pumps from the “clean” and “general” vacuum systems are each equipped with a coaxial foreline trap and a molecular sieve trap to prevent oil from reaching the turbomolecular pumps in the event of a blackout or pump malfunction. Additionally, an oil filter has been installed in the exhaust line of each of the pumps, which is then led outside of the building. They have each also been equipped with an automatic oil return line and a Pirani TPR 280<sup>8</sup> pressure gauge. To avoid the formation of a potentially explosive atmosphere at the exhaust of the vacuum pumps if hydrogen or other explosive gases are used in the ion source, each pump

<sup>7</sup>Trademark of National Lab GmbH

<sup>8</sup>Trademark of Pfeiffer Vacuum GmbH

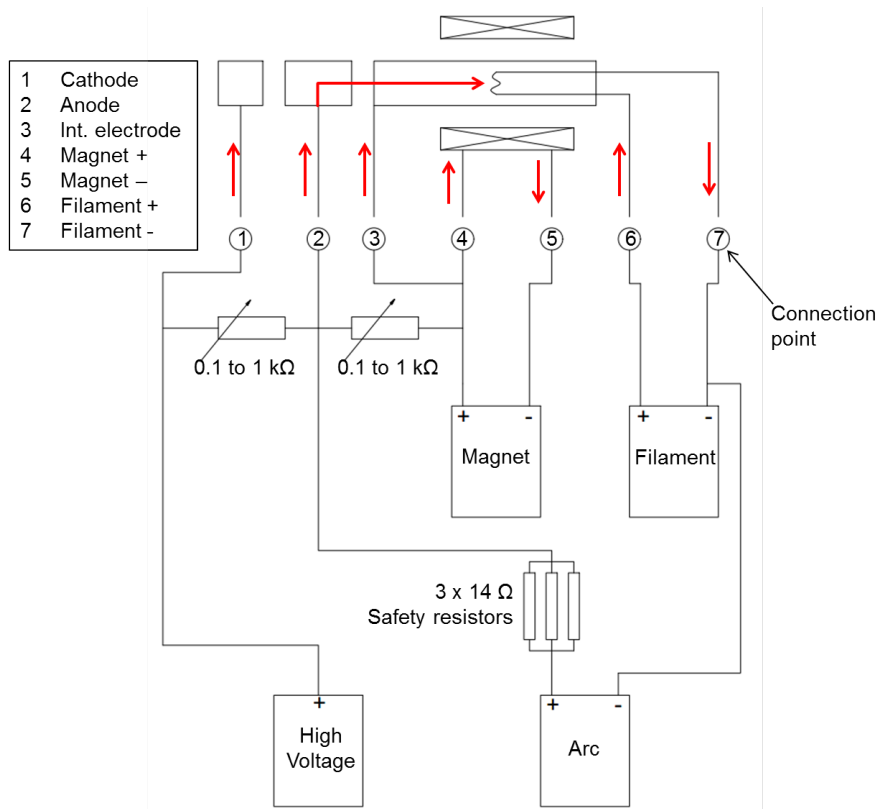


Figure 8: Schematic of the electrical connections of the DuoPIGatron ion source to the power supplies. The red arrows above the connection points represent the direction of the electric current. All connection points as well as the magnet, arc and filament power supplies are set to high voltage by way of the high voltage power supply.

### HSQ vacuum system

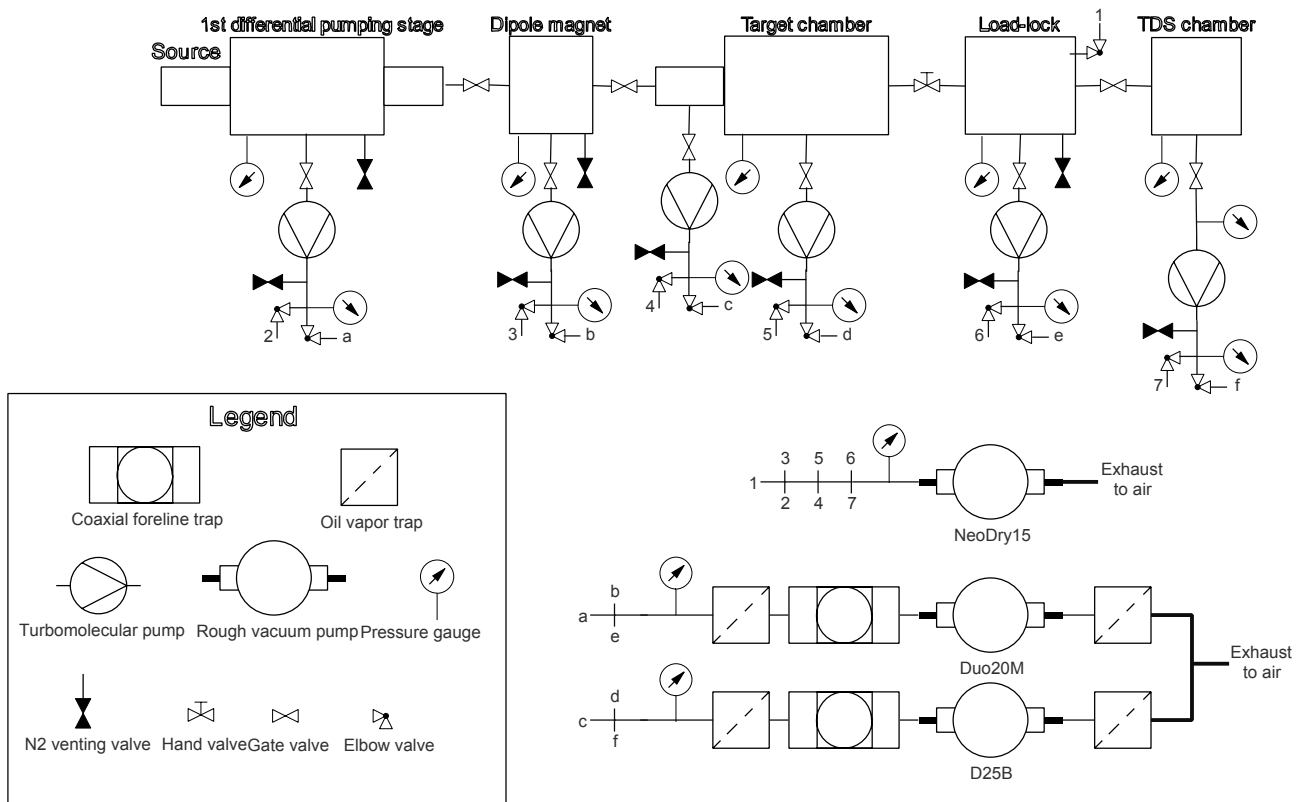


Figure 9: Schematic of the vacuum system of SIESTA.

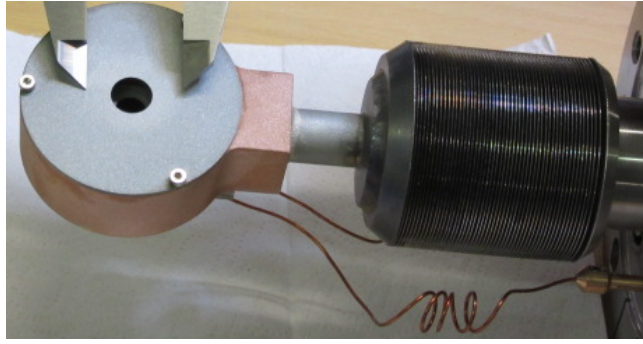


Figure 10: Beam-stopper employed at SIESTA equipped with a faraday cup to measure the ion beam current.

is provided with a gas ballast connected to an  $N_2$  line. A Duo20M rotary vane pump<sup>9</sup> is used for the “clean” vacuum system. The “general” system employs a D25B pump<sup>10</sup>. The pressure in each separate vacuum chamber is measured with a PKR 251 Full-Range Cathode<sup>11</sup>. Additionally to the Pirani gauges located at the feed of the rotary vane pumps, pirani gauges are also present at the exhaust of each turbomolecular pump in the system, after which a manual elbow valve is located. This is useful in troubleshooting situations where it is unclear whether higher than nominal pressure ( $10^{-2}$  mbar) in the rough vacuum line is due to a problem with one of the turbomolecular pumps or with the rotary vane pump it is connected to.

A base pressure of  $10^{-7}$  mbar is achieved in all the vacuum chambers. In the TDS chamber, the base pressure is below  $5 \times 10^{-9}$  mbar. Since each chamber is pumped separately and the chambers are separated by small apertures (e.g. Mo aperture, beam-defining aperture), during operation of the ion source, pressure differentials are maintained along the beam-line. The pressure in the (first) differential pumping stage is around  $10^{-4}$  mbar, the pressure at the dipole magnet (second differential pumping stage) is of the order of  $10^{-6}$  mbar and the pressure at the target chamber (third differential pumping stage) is typically around  $5 \times 10^{-7}$  mbar.

All vacuum connections in the high-vacuum chambers are made with CF<sup>12</sup> flanges, with the exception of the gas inlet (KF flanges), the  $N_2$  venting lines (KF) and the differential pumping stage flanges (ISO-K). KF connections are used in all the rough vacuum lines (between the turbomolecular pumps and the rough pumps). All gate valves are pneumatically actuated, possessing a mechanic and electric switch, with the exception of the gate valve connecting the target chamber and the load-lock. This is actuated manually as a precaution: in case of loss of power while the horizontal manipulator is fully extended into the target chamber - as is the case when switching samples - the gate valve could shut automatically, damaging the gate valve and potentially also causing damage to the manipulator and target chamber.

## 2.4 Beam-stopper

The beam-stopper, shown in more detail in fig. 10, can be inserted into the ion beam to obscure the target without shutting off the ion source. The beam-stopper is mounted on a vacuum bellows and is equipped with a pneumatic piston to extend or retract it. Additionally, the beam-stopper is also equipped with a Faraday cup (fig. 10), which allows measurement of the beam current at this position. The metal sheet with the  $\text{\O} 7$  mm aperture in front of the Faraday cup is electrically isolated from the Faraday cup and can be biased to repel electrons trapped in the beam and inhibit secondary electrons from leaving the Faraday cup. As described in section 2.2, the beam-stopper is water-cooled.

## 2.5 Dipole magnet and quadrupole lens

The dipole electromagnet was custom-made by DANFYSIK<sup>13</sup>, supplying a nominal uniform field of 0.13 T at a current of 27 A. The nominal curvature radius to deflect the ion beam towards the target is 150 mm. Operation with the magnet at higher currents is possible, up to 120 A, leading to a maximum induction of 0.7 T, enough to successfully deflect 10 keV Ar ions. To evacuate the heat resulting from the coils, the magnet is water cooled (section 2.2). Ferromagnetic yokes within the vacuum chamber of the dipole magnet (shown in fig. 11) help ensure field uniformity and reduce stray fields. The two exits are situated at  $\pm 44^\circ$  from the central axis (fig. 11). The magnet allows for symmetric deflection to either side, with the target chamber located to the right, as seen from the ion source. Another experiment, PERMEX (PERmeation EXperiment), is planned for the left exit of the dipole magnet. Mass selection at the dipole magnet is accomplished by applying a voltage to the coils

<sup>9</sup>Trademark of Pfeiffer Vacuum GmbH

<sup>10</sup>Trademark of Leybold GmbH

<sup>11</sup>Trademark of Pfeiffer Vacuum GmbH

<sup>12</sup>ConFlat is a registered trademark of Varian, Inc.

<sup>13</sup>Registered trademark

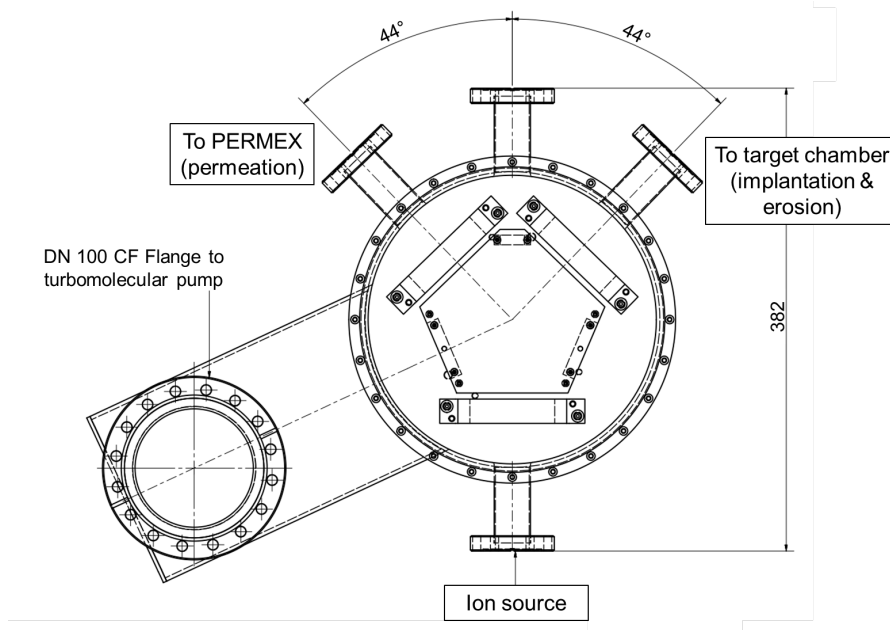


Figure 11: Half section cut of the dipole magnet. The beam enters the magnet through the lower CF40 flange and can be deflected either left or right, depending on the direction of the magnetic field, so that the desired ion species exits the magnet through the corresponding CF 40 flange. Magnetic yokes are present inside the vacuum chamber to increase the uniformity of the magnetic field at the center of the magnet. The shaft on the left connects through a CF 100 flange to a turbomolecular pump, improving pumping of the chamber.

of the electromagnet, thereby producing a current which induces the desired magnetic field within the shunt regions. This will induce a curvature in the particle trajectories within the magnetic sector field, as described by the Lorentz force. In the case of SIESTA, the ion beam is mono-energetic, so by varying the applied voltage to the coils, the magnetic field can be chosen such that only the trajectories of ions of a certain mass exit the magnetic sector field and reach the target. If  $q$ ,  $m$  and  $E$  are respectively the charge, mass and kinetic energy of the particle,  $\vec{v}$  is the velocity of the particle,  $\vec{B}$  is the applied magnetic field and  $r$  is the radius, then setting  $\vec{F}_{Lorentz} = \vec{F}_{centripetal}$ , yields:

$$q \cdot \vec{v} \times \vec{B} = \frac{m \cdot |\vec{v}|^2}{r}. \quad (4)$$

Treating the equation as a scalar (applicable in this case since  $\vec{v}$  and  $\vec{B}$  are perpendicular), it can be seen that:

$$Br = \frac{mv}{q} = \frac{p}{q} = R, \quad (5)$$

where  $p$  is the momentum of the ion.  $R$  is known as the rigidity, and is a measure of the resistance of an ion to deflection. Applying  $E = \frac{1}{2}mv^2 \rightarrow v = \sqrt{\frac{2E}{m}}$  with  $E$  the kinetic energy of the particle yields:

$$R = Br = \frac{\sqrt{2Em}}{q}, \quad (6)$$

where  $R$  is the rigidity of the ion. Since in SIESTA the radius of curvature is constant, equal to 150 cm and, within error due to magnetic hysteresis,  $\|\vec{B}\| \propto I$ , with  $I$  the current through the dipole magnet:

$$I \propto R. \quad (7)$$

Consequently, for a given ion energy (chosen by setting the desired extraction potential at the ion source), the current which must pass through the magnet coils in order to deflect the desired ion species to the target will be directly proportional to the square root of the mass of the ions.

An ion passing through a deflector magnet will also be focused in the plane of deflection. As a consequence of this, downstream from the magnet an initially circular beam will have an elliptic cross section, with a different beam emittance in the horizontal and vertical plane. In order to increase the flux density at the target, a magnetic quadrupole doublet lens consisting of two QM-60.100 quadrupoles from D-Pace<sup>14</sup> (shown in fig. 12) was installed between dipole magnet and target chamber, as this lens allows for different foci in the horizontal and vertical plane [13].

<sup>14</sup>Registered trademark

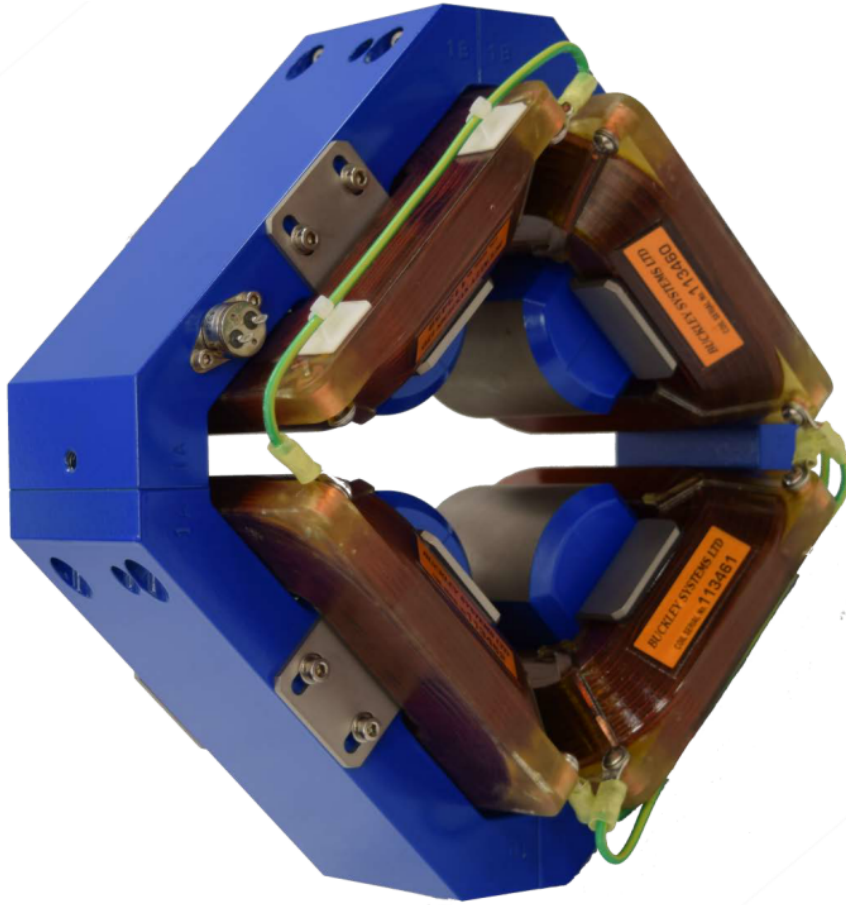


Figure 12: QM-60.100 Quadrupole lens from D-Pace employed in SIESTA.

## 2.6 Target chamber and load-lock

The target chamber is divided into two connected volumes: an antechamber with a length of 130 mm along the beam axis equipped with its own turbomolecular pump for improved differential pumping; and the main target chamber housing the sample to be exposed. The sample is placed within a cylindrical double cage, which is required for an accurate measurement of the ion-beam current under all operating conditions, as explained in more detail later in this section. The two volumes are connected by a tube of 46.8 mm in diameter. A beam-defining aperture is situated in the target chamber at the exit of this tube, and is described in more detail later in this section. The ion beam propagates along the axis of this tube towards the target, passing through the beam-defining aperture and two aligned diaphragms in the double cage before impinging on the target sample. The sample is fitted into a specifically-designed tripod, which rests atop a platform with each leg fitting on a cylinder. The platform can be rotated relative to the ion beam to alter the angle of incidence and can be moved in the vertical direction to adjust the height of the beam footprint on the sample. The manipulator is also used to mount the sample on the target platform from the load-lock. If a different ion energy at the target than the extracted energy is desired, the sample may be biased to  $\pm 6$  kV. The general setup, without beam defining aperture, is shown in fig. 13.

Additionally, the sample can be heated from its backside by electron impact. This is enabled by employing a filament located behind the sample: a current is passed through this filament to heat it, emitting electrons through thermionic emission. A potential difference is applied between the target and the filament, accelerating the emitted electrons towards the target. This electron current will heat up the target to temperatures of up to 1300 K. Radiative heating from the filament of the electron gun plays a role at moderate temperatures, and can be neglected at higher temperatures when compared to the power output of electron impact heating. The filament is taken from a P21W 12 V, 21 W OSRAM<sup>15</sup> light bulb. To improve the heating efficiency, a metallic cup surrounds the filament. This heating cup is electrically connected to the filament, shielding the filament from all other external fields and effectively “directing” the emitted electrons towards the target. This can be accomplished by either biasing the target to a positive potential, or by biasing the filament negatively and leaving the target grounded. The heating filament, cup and target holder (with target) can be seen in fig. 14.

The temperature is measured with a type-K thermocouple connected to the target through the two hind

<sup>15</sup>Trademark of OSRAM GmbH

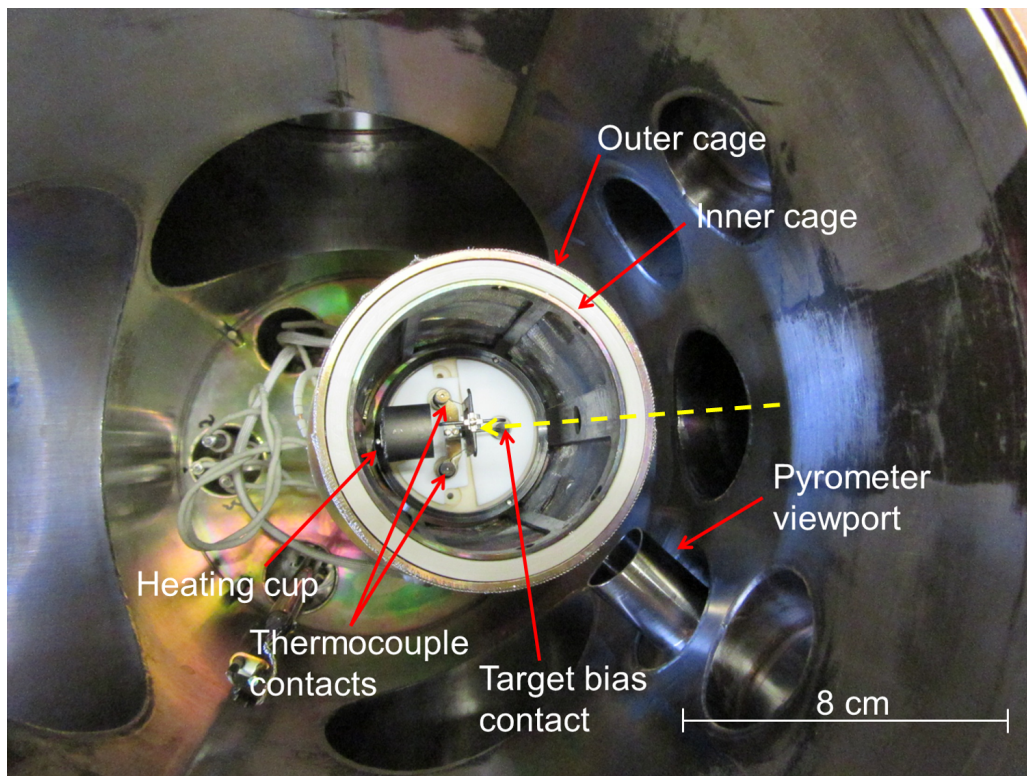


Figure 13: Top view of target chamber interior showing the double cage, pyrometer viewport, heating cup and target holder with thermocouple and target bias contacts. The beam defining aperture is absent. The beam direction is from right to left as indicated by the yellow dashed arrow.

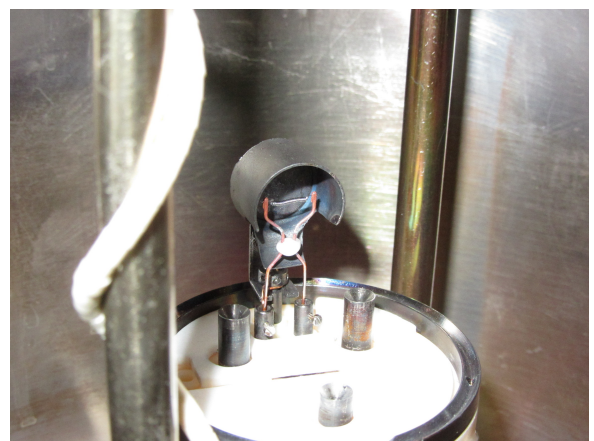


Figure 14: Target platform with heating filament, with (left) and without target (right). The two hind legs of the target holder are connected to a type-K thermocouple. The front leg is connected to a power supply which sets the bias of the sample. The heating cup is electrically connected to the heating filament. The hooks situated on top of the target holder are used to weigh the sample and to transport it between target chamber, load-lock and TDS chamber.

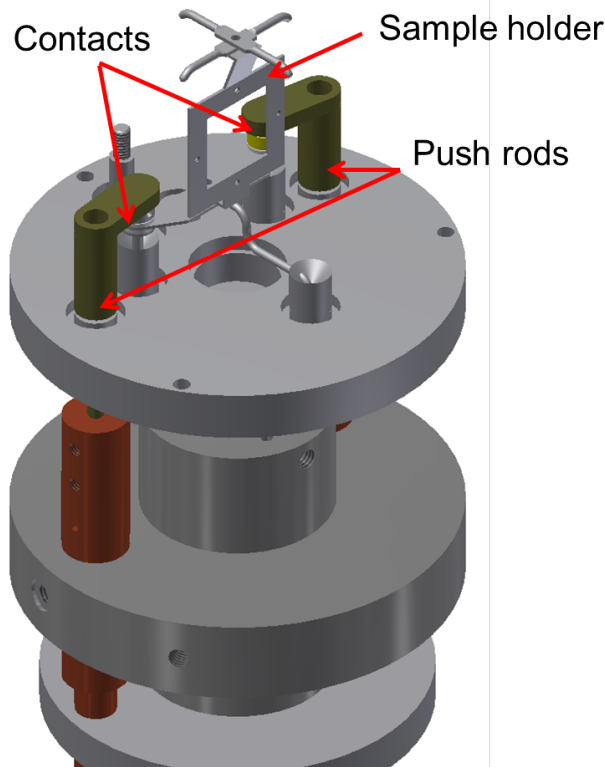


Figure 15: Push rods can be used to press down on the sample holder hind legs, thereby improving the electrical contact between thermocouple contacts and the target.

legs of the tripod sample holder. In order to improve contact between the target and the thermocouple, two push rods (not shown in fig. 13) can be used to press down on the hind legs of the sample holder. These rods are located on the left and right side of the target platform, i.e., on either side of the sample holder, and are outfitted with springs to apply a downwards force on the target holder legs. The push rods are shown in fig. 15. Since the thermocouple is in electrical contact with the target, it is also biased to the same potential as the target. The thermocouple display electronics is at ground potential. If the thermocouple were connected directly to the display electronics, it would short-circuit the target bias power supply, potentially damaging the equipment and constituting an electrical hazard. The biased thermocouple signal is transmitted to the grounded display electronics via a voltage-to-frequency converter (on the thermocouple end), a fiber-optic wave-guide and a frequency-to-voltage converter (on the display electronics end). A Maurer type TMRS 95/105<sup>16</sup> infrared pyrometer with a measuring range of 50°C - 1000°C is located outside the vacuum chamber and also has direct line of sight to the target, allowing for a second independent temperature measurement. The target heating filament was tested at a target bias of 3kV with filament currents between 0 and 1.6 A. At 1.6 A, an electron current reaching the target of 21 mA was measured, from which a heating power of 63 W can be calculated.

The ion current reaching the target must be measured accurately, as this is required to determine the ion flux. Secondary electrons are emitted when the ion beam impinges on the target, potentially being registered as an additional positive current. The current measurement would thus be overestimated. If the sample is positively biased, low-energy electrons that are trapped in the potential well of the positive ion beam would be accelerated towards the target, leading again to an erroneous current measurement, this time underestimating the ion current. To avoid both of these issues, the outer cage surrounding the target is set to a low negative bias (-10 V) and the inner cage is included in the current measurement and grounded. With this setup, electrons trapped in the potential well of the beam are repelled by the outer cage and so do not reach the target, whereas those emitted at the target are collected by the grounded inner cage and included in the current measurement.

If the sample is heated during ion irradiation, the electron current to the target backside will constitute an additional negative current. Typically, this current is orders of magnitude larger than the impinging ion current ( $\mu\text{A}$  vs. mA). To allow accurate measurement of the ion current, one end of the filament is also connected to the current measurement. This way, the “electron current circuit” is closed and no current due to electrons from the heating filament is registered at the current measurement. The contact point of the grounded current integrator will differ, depending on whether the target is biased positively and the filament is grounded (connection scheme A, fig. 16), or the target is connected to the 0 V connection point of the high-voltage power supply and the filament is set to a negative bias (connection scheme B, fig. 16).

<sup>16</sup>Trademark of Dr. Georg Maurer GmbH Optoelektronik.

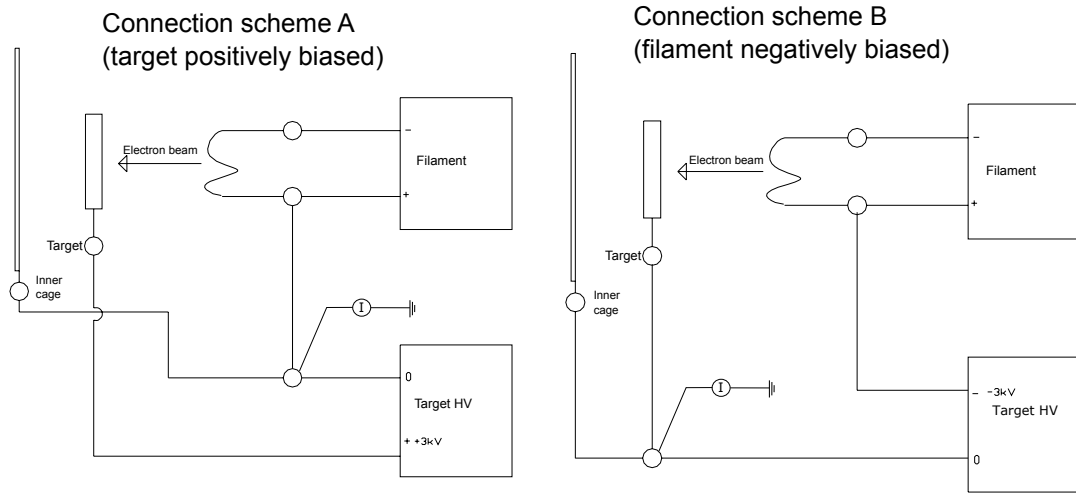


Figure 16: Connection schemes for the target chamber of SIESTA, allowing for the target to be positively biased and the heating filament set to ground potential (A), or conversely for the target to be grounded and the heating filament set to a negative bias (B). In both cases the ion beam impinges on the target from the left, passing through a hole in the grounded inner cage. A current integrator, labeled “T”, is used to measure the ion current.

Finally, during operation it is occasionally useful to measure the ion beam current at the target without exposing the sample. This is of use for example when tuning the dipole magnet current before exposure. Since the cup surrounding the heating filament is also connected to the current measurement, this can be achieved by rotating the target platform 180°, in which case the ion beam impinges on the back of the heating cup. The ion current is thereby measured accurately at the target and the dipole magnet, gas flow, etc., can be adjusted before exposing the sample. When all systems have been correctly tuned, the target platform can be rotated back 180° to commence exposure of the sample to the ion beam. A high-voltage switchboard is used to alter the connection scheme of all of the components as desired, allowing for other connection schemes than the ones mentioned if needed. Since all the electrical connections may be set to a high voltage using the switchboard, grounded aluminum caps have been fastened around the electrical connections at the target chamber, preventing any possible contact with the high voltage components. Additionally, a door with a grating has also been installed under the target chamber. A relay connected to the high-voltage power supply is attached to the door-frame, so that if the door is opened - for instance to access the vertical manipulator - the high-voltage power supply for the target is automatically switched off.

The beam-defining aperture, located between the outer cage and the tube connecting main target chamber and antechamber (shown in fig. 1), consists of a molybdenum plate with a series of holes and slits of different sizes aligned vertically along its axis. The plate is screwed to a vertical manipulator located above the target platform. By adjusting the height of the plate, the desired shape of the beam-defining aperture can be selected. Circular holes with diameters of 4, 5 and 6 mm are available, as are vertically elongated stadiums with dimensions of 1.5x6, 2x6 and 3x6 mm. The beam-defining aperture can be seen in its installed position in fig. 17. In order to avoid contact of the ion beam with the inner and outer cages, the outer cage hole diameter is 8 mm and the inner cage hole has a diameter 9.3 mm. The beam footprint at the beam-defining aperture can be large enough to encompass more than one of the holes. If this were to happen, part of the beam would not only impinge on the sample, but also needlessly erode the cages, possibly affecting the current measurement. To avoid this, a thin plate has been installed between the beam defining aperture and the tube connecting the two vacuum volumes, with a hole 12 mm in diameter aligned with the ion beam trajectory. The plate covers the rest of the tube connecting the antechamber and the target chamber, so that all the lines of sight between the ion beam and the target chamber pass through only one hole of beam-defining aperture.

A magnetically-coupled suspension balance is located directly above the target chamber. Before or after exposure in SIESTA, a sample may be hung from the measuring hooks of the balance and weighed in-situ. The measurement procedure of the microbalance is described in more detail in section 3.6.

## 2.7 Load-lock

The load-lock enables the quick and easy exchange of samples in the target chamber by limiting the volume to be vented and re-evacuated during the procedure to the load-lock vacuum chamber. As can be seen in fig. 14, two pairs of hooks are situated on top of the target holder. They are used to transport the sample to and from

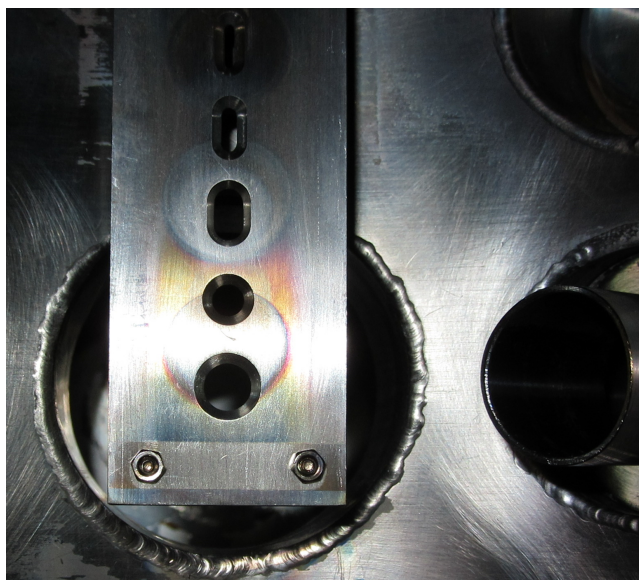


Figure 17: Beam defining aperture in the target chamber. In the picture, the bottom hole is aligned with the ion beam trajectory. The thin plate installed between beam defining aperture and connecting tube to the antechamber is not present. The tube on the right provides a line of sight between the pyrometer and the sample.

the target chamber through the manually operated CF 100 gate valve that connects the target chamber and the load-lock. To vent the load-lock, all gate valves (between target chamber and load-lock, load-lock and TDS and Load-lock to turbomolecular pump) are closed and the elbow valve connected to the  $N_2$  line is opened.

The sample, already mounted on the target holder, can then be inserted by hanging it on the hooks of the horizontal manipulator. The  $N_2$  elbow valve and load-lock door are then closed and the elbow valve leading to the bypass pump is opened. At this point the vacuum vessel can be evacuated via the bypass until a pressure of  $5 \cdot 10^{-2}$  mbar is achieved. The elbow valve connecting the bypass pump to the load-lock vacuum chamber is then closed and the pump is switched off. The gate valve leading to the turbomolecular pump can then be re-opened. When a pressure of  $10^{-4}$  mbar is achieved, the manually operated gate valve leading to the target chamber is once again opened and the horizontal manipulator is used to slide the sample into the target chamber. The vertical manipulator on the target platform must also be used to correctly “seat” the sample holder on the three hollow cylinders. Failure to position the sample adequately can lead to errors in the current and temperature measurements.

To extract a sample from the target chamber, the same procedure is followed in reverse. When performed correctly, an old sample can be exchanged for the next one to be irradiated in under 10 minutes. During this time, the ion source can be left “running”. However, to protect the inside of the target chamber, it is strongly advised to leave the beam-stopper inserted during the whole sample exchange procedure.

The load lock is equipped with four external screws with springs. While under vacuum, at least one of the screws of the load-lock should be screwed in, though only loosely. During venting, if the screws are not screwed in too tightly, the load-lock will partly open when it reaches atmospheric pressure. If no screw is screwed in, the door is liable to open violently, potentially damaging nearby users or equipment. If one or more screws are screwed in too tightly and the  $N_2$  venting line is set to a pressure above 1.2 bar, pressure could continue to rise in the load-lock above atmospheric pressure, potentially causing the load-lock view-port to burst. To avoid this, the pressure in the  $N_2$  line is regulated to always be below 1.2 bar.

## 2.8 In-situ thermal desorption spectrometry

A thermal desorption spectroscopy chamber is located directly below the load lock. As with the target chamber, a manipulator - in this case vertical - is equipped with a hook and is used to transfer a sample from the load-lock to the TDS chamber. A thermocouple and heating mechanism identical to the ones in the target chamber are employed to heat up the sample to temperatures of more than 1000 K. A PID system may be used to control the sample temperature. A quadrupole mass spectrometer (QMS) is situated a distance of approximately 6 cm from the sample with direct line of sight. With this setup, a previously-loaded sample may be de-gassed at high temperatures and the released gas composition will be measured by the QMS, leading to information about the gas retention properties of the sample. A base pressure of under  $5 \cdot 10^{-9}$  mbar is achieved with a dedicated turbomolecular pump. The TDS chamber is also equipped with a liquid nitrogen getter pump, helping to reduce the pressure during operation. The sample platform with heating cup and quadrupole mass spectrometer are

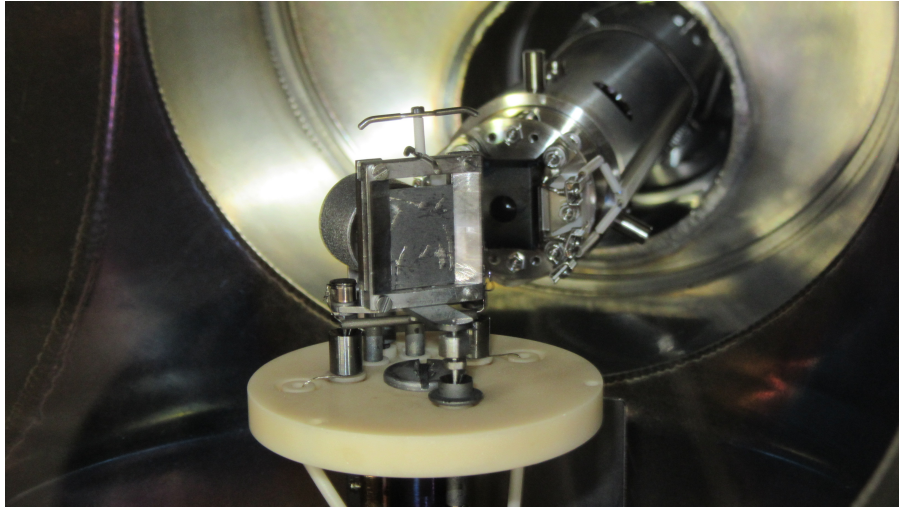


Figure 18: Target holder with sample in TDS chamber. The sample can be biased and can be heated by a filament located at the backside of the sample, providing electron impact heating. The quadrupole mass spectrometer, located behind the target holder, is used to analyze the composition of the gas that is desorbed from the sample.

shown in fig. 18

Since the sample is also heated via electron-impact heating, another dedicated power supply is used to bias the target up to 6 kV. As in the case of the target chamber, the thermocouple measuring the temperature at the sample is also biased and aluminum caps have been installed to prevent contact with the electrical connections of the TDS chamber. Since the load-lock is connected to both the target chamber and TDS chamber, a sample can be irradiated and taken to the TDS chamber to be analyzed without the need to vent at any point, allowing for in-vacuo TDS of irradiated samples.

## 3 Characterization

### 3.1 Mapping of source parameters

The ion source was fully characterized for use with deuterium. Hydrogen (protium) hydrogen-helium and hydrogen-argon plasmas were also successfully produced. The latter two behave similarly to hydrogen and deuterium, unless stated otherwise.

With the goal of maximizing the ion current reaching the target, parameter scans were performed to study the effect on the ion current of the extraction voltage, the pressure in the differential pumping stage (controlled by varying the neutral gas throughput) and the ion source magnet, filament and arc currents. Additionally, the optimal pressure in the differential pumping stage and the optimal intermediate grid voltage were also systematically studied as a function of the extraction voltage. For these tests, the ion current was measured with the Faraday cup located at the beam-stopper, between the differential pumping stage and the dipole magnet (figs. 1 and 10). The measuring cup was set to ground potential, while the aperture in front of the cup was set to a negative bias of -25 V to repel thermal electrons trapped in the potential well of the ion beam and to deflect secondary electrons emitted at the measuring cup back towards the cup. A vertical cross section of the beam profile was measured with an aperture of  $\varnothing$  1 mm as explained further below.

The parameters detailed in table 1 were taken as reference values: whenever any of the parameters were varied, the other parameters were set to the values listed in the table. These reference values were obtained from earlier experience with the precursor of SIESTA, the HSQ [5], as there they were proven to enable reliable, steady state operation while fulfilling the experimental requirements of the device. However, it must be noted that even employing the same set of parameters, the same ion current measured at the beam-stopper was not always obtained. Differences in the measured current of up to 20% were observed, which could be attributed to the conditioning of the source for use with a certain gas species and the “aging” of the coating on the filament, which degrades over time and affects the long-term stability of the beam.

The measuring procedure was in general as follows:

1. The beam-stopper (Faraday cup) was inserted and the  $\varnothing$  7 mm aperture in front of the cup was set to -25 V.
2. The desired extraction voltage was set, as were the operating currents of the ion source magnet, filament and arc. The ion source magnet, filament and arc voltages were allowed to vary.

Element	Voltage relative extraction voltage (= 6010 V) [V]	Current [A]
Cathode	0	0.12
Anode	+20	11.7
Intermediate electrode	-30	0.28
Magnet +	-30	30.5
Magnet -	-40	30.5
Filament +	-24	8.1
Filament -	-27	20.3

Table 2: Measured voltages and currents at the several contact points of the ion source (fig. 8). Voltages shown are relative to the cathode (plasma grid) voltage, which was 6 kV. Currents are measured in the direction indicated by the arrows above the connection points in fig. 8. The voltages and currents applied by the power supplies under the same conditions are listed in tab. 1.

- Gas was let into the source through the flow controller until the arc current increased to the desired level, prompting an ion current being measured by the Faraday cup at the beam-stopper. The arc was not yet stable, as evidenced by oscillations in the arc voltage of the order of 50 V. These oscillations diminished over time without any action being required within 1 - 2 minutes.
- Once the arc current was stable (indicating the source was now running in steady state), the (negative) intermediate grid voltage was increased, leading to a rapid increase of the ion current measured by the Faraday cup. Once the negative voltage had increased to a certain level, the ion current would reach a maximum. Beyond this point, further increase of the negative intermediate grid bias potential led to a slight decrease in the measured ion current. The voltage at which the ion current reached its maximum was noted as the optimal intermediate grid voltage.
- The gas flow into the source through the flow controllers was then varied while the arc was maintained at the desired operating current. An optimal gas flow was found which led to the highest ion current at the beam stopper. The pressure at the first differential pumping stage and the maximum measured ion current were recorded.

For the following tests, deuterium was used. The voltages at each point shown in figure 8 were measured relative to the cathode (plasma grid) voltage of 6 kV. The electric currents were also measured at each connection point, in the direction depicted by the red arrows above the connection points in the diagram. During these measurements (table 2), the ion source was operated at the source parameters shown in table 1 (see section 2.2). The arc current can be calculated as the difference between the filament currents at the + and - connections, equaling in this case 12.2 A. This current reaches the anode (11.7 A), intermediate electrode (0.28 A) and the extraction grid (0.12 A). The measurements agree with the displayed values of the power supplies within the measurement uncertainties.

Fig. 19 shows the maximum ion current measured with the Faraday cup at the beam-stopper with the extraction voltage ranging from 0.7 to 15 kV when optimizing the gas flow to the ion source. The data were fitted by applying equation 2 with constant perveance, showing good agreement. It must be noted that the Child-Langmuir law only describes the current that is extracted from the source (eq. 1), while the data points correspond to the current measured at the beam stopper, i.e., after the beam has passed through the differential pumping stage and has been partly cut off by the Mo aperture. Under these conditions, the current through the source magnet, filament or arc show no effect on the extracted ion current within the experimental uncertainty, as can be observed in figure 20. However, the source is not space-charge limited, since the perveance of the source is significantly smaller than the maximum perveance given by the Child-Langmuir law (eqs. 1 & 2) and the ion current emitted from the source varies with the gas throughput (fig. 22).

The correlation of the optimal intermediate grid voltage with the extraction voltage was also investigated (fig. 21). The negative potential at the intermediate grid must be strong enough to repel back-streaming electrons, “screening” the ion source, without de-focusing the ion beam too strongly. The required potential to accomplish this should, therefore, be directly proportional to the extraction potential and inversely proportional to the gap between grids, which is constant ( $U_{intermediate} \propto U_{extraction}$ ). This was experimentally confirmed, with a strongly linear relationship between the extraction and optimal intermediate grid voltages being observed, i.e., the optimal grid voltage is a constant fraction of the extraction voltage (approximately 0.01).

The ion current variation around the optimal pressure in the differential pumping stage was also studied. Figure 22 shows the ion current emitted from the source (measured at the extraction voltage power supply) divided by 1000, the ion current measured with the Faraday cup at the beam-stopper when using an aperture of  $\varnothing 5$  mm and the ion current measured at the target chamber, plotted as a function the gas pressure in the

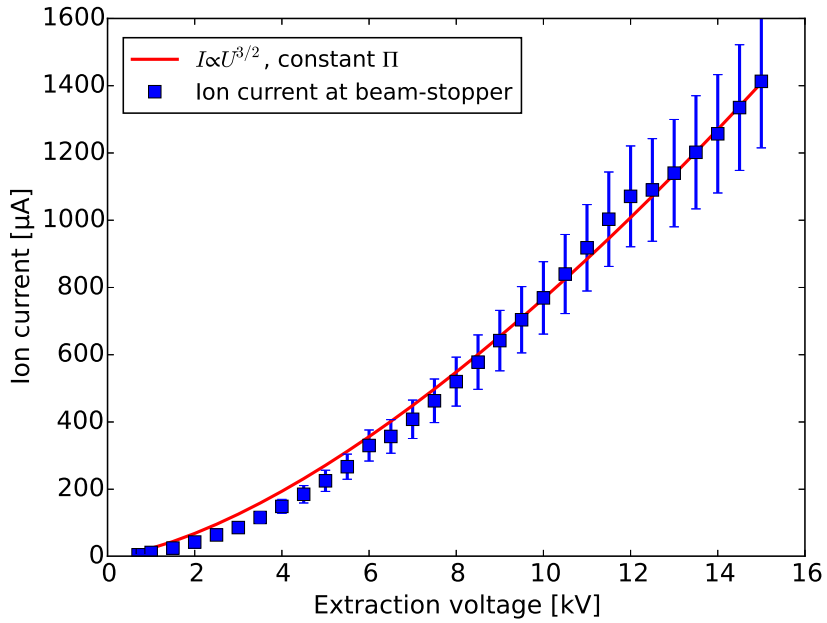


Figure 19: Ion current measured at the beam-stopper with increasing extraction voltage, fitted with a curve of constant perveance as described in eq. 2 [9]. The increase in the size of the error bars for ion currents above 1 mA is due to a change in the measurement range of the current integrator.

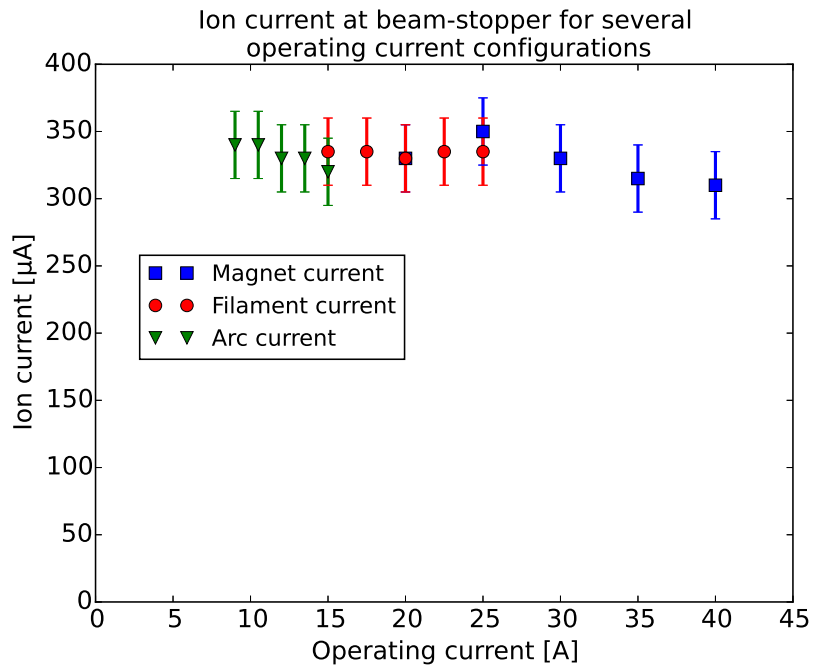


Figure 20: Ion current measured at the beam-stopper with the source magnet, filament and arc set to various operating currents, with all other parameters set to maximize ion current. Within the error of the experimental measurement, no effect of these parameters on the extracted ion current could be observed.

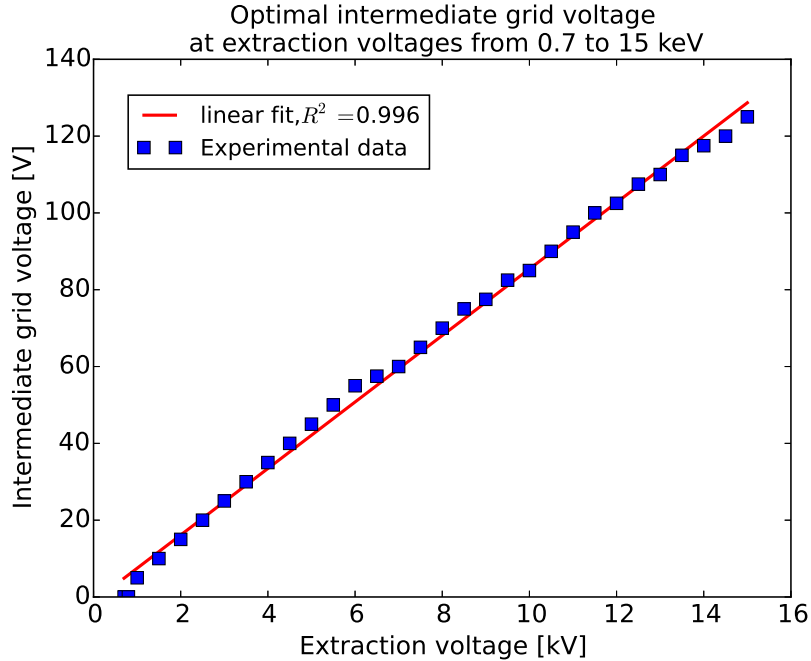


Figure 21: Optimal intermediate grid voltage (negative) for increasing extraction voltages. The error bars for the experimental values are smaller than the size of the markers.

differential pumping stage when extracting a 6 keV  $D_3^+$  beam. The currents are measured at different positions with differing beam-defining apertures and beam optics, and therefore cannot be directly compared with one another. For instance, the current measured at the beam-stopper Faraday cup through the  $\varnothing 5$  mm aperture is approximately 10% of the current that passes through the  $\varnothing 16$  mm Mo aperture, as can be estimated from the beam profile at the beam-stopper shown in fig. 26 and discussed further in this section. Due to the focusing effect of the quadrupole lenses, and the fact that the beam-defining aperture at the target is larger than the one used at the Faraday cup, the ion current measured at the target is larger than the current measured at the Faraday cup. Below a pressure of approximately  $4 \cdot 10^{-5}$  mbar, the ion source cannot be operated reliably because the arc discharge in the ion source becomes unstable. Given the trend of the curve towards higher extracted ion currents at lower gas pressures, it can be assumed that a space-charge limited regime would be reached if the pressure in the plasma source could be further reduced. However, this cannot be achieved with the current plasma feed, since at lower gas pressures the DuoPIGatron source is not able to maintain the plasma discharge. A pressure optimum is observed for the ion current measurement at the beam-stopper Faraday cup and at the target. At pressures below this optimum, a higher current is extracted from the ion source, but due to increased beam divergence, a large fraction of the beam impinges on the Mo aperture and, in the case of the measurement at the target, the vacuum tubes at the entrance and exit of the dipole magnet. This increase in beam divergence occurs in the ion extraction stage (gap between plasma and grounded grids) and between the grounded grid and the measurement point due to insufficient space-charge compensation at the exit of the ion source [9]. Near the pressure optimum, the beam achieves a high degree of space-charge compensation, which leads to a relatively low divergence. The pressure optimum is at slightly lower pressure for the current measured at the beam-stopper Faraday cup than for the ion current measured at the target. This can be explained by the smaller distance between measurement point and ion source. Because the beam stopper Faraday cup is much closer to the source than the target, the current at this position is less influenced by beam divergence. The increase in the loss of current due to insufficient space charge compensation is partially overcompensated by the increase of ion current extracted from the ion source. At pressures higher than the optimum, the beam is already highly space-charge compensated. A further increase of pressure leads to a decrease of current due to beam neutralization.

It was observed that the pressure optima vary slightly on a day to day basis. This could be due to the reproducibility of the Full-Range Cold Cathode pressure gauges used, and does not seem to depend heavily on the extraction voltage, as can be seen in fig. 23. The pressure optimum was typically around  $10^{-4}$  mbar. Dependences between the intermediate grid voltage and the pressure optimum and other source parameters (current through ion source magnet, filament and arc current) were also tested, but none were found.

To test the flow controllers, the gas pressure at the differential pumping stage was measured while increasing the flow controller nominal gas throughput, showing a linear increase with the throughput, as is shown in fig. 24, indicating that the flow controllers can be used to reliably adjust the gas pressure at the differential pumping stage.

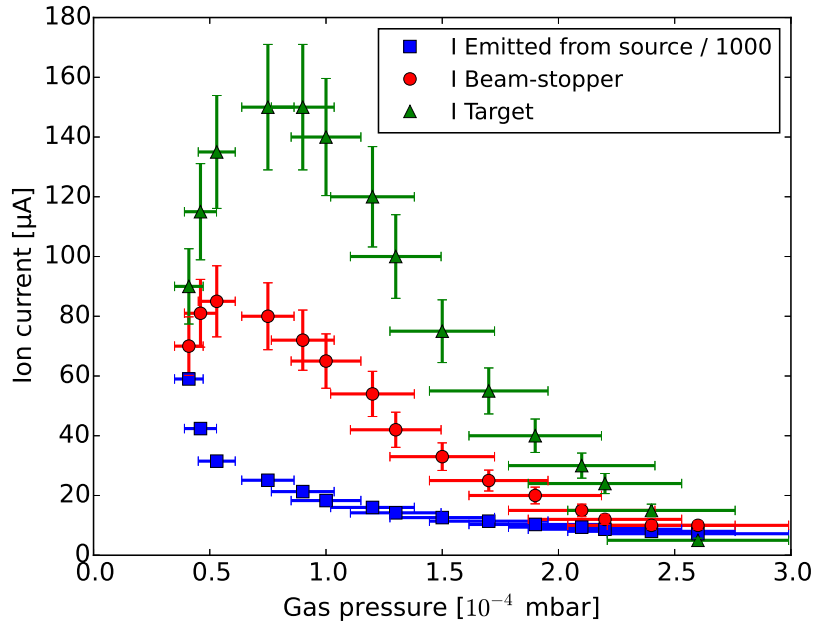


Figure 22: Ion current from a 6 kV  $D_3^+$  beam measured at the exit of the ion source (divided by 1000, squares), at the beam-stopper Faraday cup (circles) and at the target (triangles) as a function of pressure in the first differential pumping stage. The ion current measured by the beam-stopper Faraday cup and at the target shows a peak at a specific pressure “optimum” for a given discharge. No optimum is observed for the ion current emitted from the source. A larger current is measured at the target because the beam is focused before reaching the target and the beam-defining aperture at the target is larger than the one used at the Faraday cup.

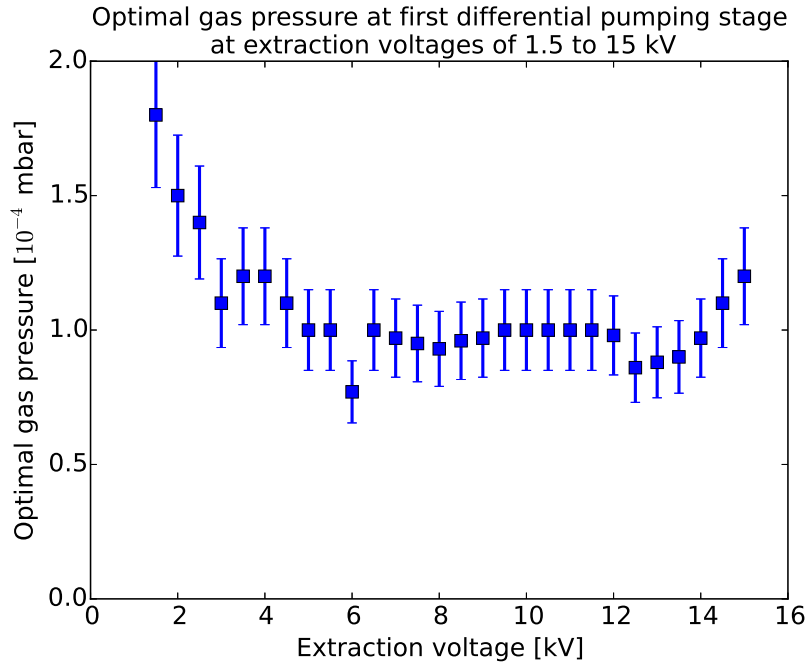


Figure 23: Optimal gas pressure with increasing extraction voltage when using deuterium. For extraction voltages below 4 kV, lower extraction voltages lead to a higher optimal gas pressure. For voltages of or above 4 kV, the pressure optimum is typically in the range of  $10^{-4}$  mbar.

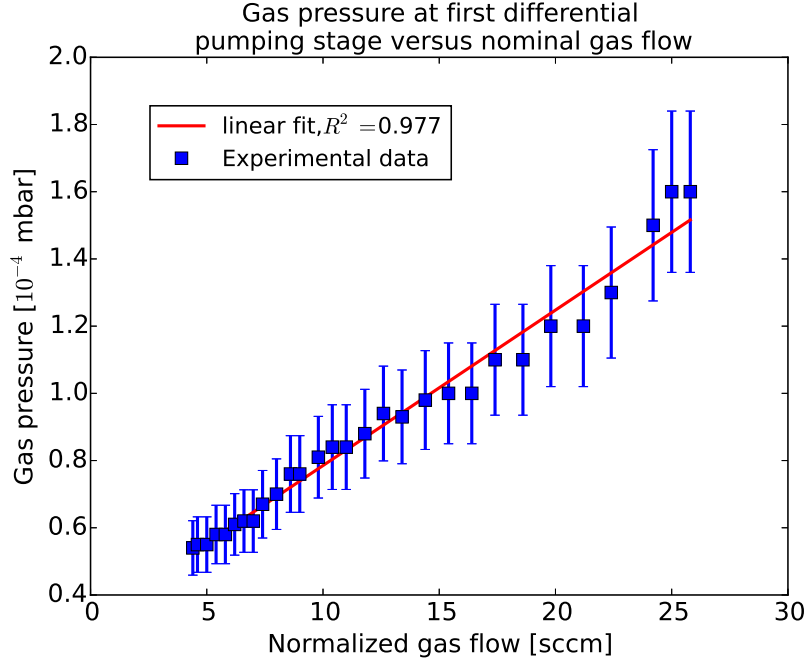


Figure 24: Gas pressure at the first differential pumping stage is plotted versus the flow-controller gas throughput. A linear regression was added, providing a good fit within the experimental error of the gas pressure measurement.

As stated before, the Faraday cup at the beam-stopper is typically grounded and the insulated aperture in front of the Faraday cup is negatively biased to repel secondary electrons and electrons trapped in the ion beam’s potential well. To understand the effect of the potentials of the Faraday cup and insulated aperture on the ion current measurement, the ion current was measured while the aperture was set to varying negative potentials, with the Faraday cup grounded or set to +36 V. This can be seen in fig. 25, which shows that at aperture bias potentials close to ground potential, measurements diverge when the Faraday cup is grounded or positively biased. Electrons trapped in the potential well of the ion beam or secondary electrons produced at the beam-stopper aperture may impinge on the Faraday cup, being registered as a “negative” current and therefore reducing the measured ion current. When the cup is grounded however, an additional effect may be observed: secondary electrons are emitted from the cup due to ion impact and are not repelled back into the cup by the insulated aperture, constituting an additional “positive” current. In this scenario, this second effect dominates, and so a higher current is measured, leading to an overestimation of the real ion current. These two competing effects can be eliminated by increasing the bias voltage applied at the aperture in front of the Faraday cup. If the aperture is sufficiently negatively biased, it will deflect the secondary electrons emitted at the Faraday cup back to the cup, so that the current is not overestimated, while repelling the electrons trapped in the potential well of the beam, so that the current is not underestimated either. At aperture bias voltages greater than -15 V, secondary electrons are retained in the Faraday cup and electrons trapped in the potential well of the beam are repelled from the cup. In this case, no difference is observed between a grounded Faraday cup and one set to +36 V. Based on these findings, it was decided to operate the beam-stopper with a grounded Faraday cup and at a bias voltage for the aperture of -25 V.

To measure the beam profile at the beam-stopper, a negatively biased aperture of  $\varnothing$  1 mm was installed onto the installed Faraday cup. The vertical position of the beam-stopper was then varied, to measure the off-axis current density of the beam, leading to line scan through the beam. Given the rotational symmetry of the ion source and extraction grids, the beam is also assumed to be cylindrically symmetric. The measured beam profile is shown in fig. 26. The ion current density appears to have a uniform value around the beam axis of  $\sim 3 \mu\text{A}/\text{mm}^2$ . Beyond a diameter of 16 mm, the ion current density drops quickly to zero. The width of the beam “edge” at this position is approximately 2 mm.

The ion source behaves similarly when operating with hydrogen (protium), with the exception of the optimal operating pressure in the first differential pumping stage, which is increased to about  $2 \times 10^{-4}$  mbar. The source cannot be ignited if helium is used as working gas. For this reason, in order to produce a He beam, the source was ignited with hydrogen and then helium was admixed through the second flow controller, up to a flow ratio of 1:1. The optimal pressure is in this case not affected by the helium concentration. The He ions are then mass selected in the magnetic sector field which is explained in the following section (sec. 3.2). It is worth noting that a helium-containing ion beam can also be achieved by first igniting the source with deuterium. However, in this case  $D_2^+$  ions will have a very similar mass as  $He^+$  ions, so the two ion species will not be mass-separated

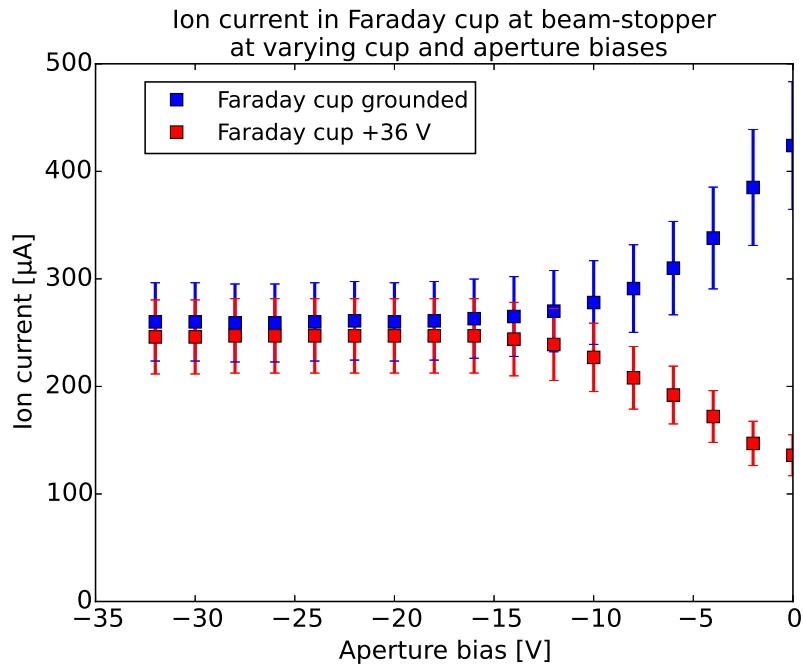


Figure 25: Ion current measurement at the beam-stopper Faraday cup with varying bias at the aperture in front of the Faraday cup and the cup either grounded or positively biased. For low (or no) aperture bias, the grounded Faraday cup leads to higher ion current measurements. Conversely, if the Faraday cup is set to a positive bias, the measured current is reduced. When a negative bias of 15 V or greater is applied at the aperture in front of the Faraday cup, whether the cup is biased or grounded does not play a role in the ion current measurement.

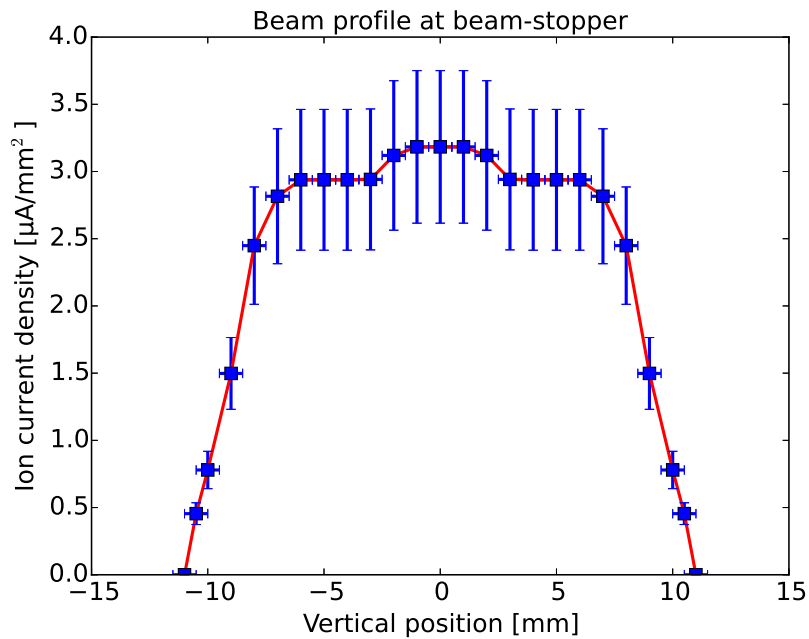


Figure 26: Beam profile at beam-stopper measured with Faraday cup. A line has been added to guide the eye. The ion current density appears to be uniform near the beam axis within the uncertainty of the measurement, with an edge width of approx. 2 mm.

when passing through the dipole magnet.

As with helium, the source does not ignite with argon. Similarly, the source must be ignited with hydrogen or deuterium and argon must then be admixed to produce an Ar beam. It must be noted that argon degrades the coating of the filament in a matter of hours. This coating is sputtered onto the ceramic insulators, which become slightly electrically conductive. Depending on the desired Ar fluence to be achieved, the filament may have to be re-coated. Because of this, long-term operation with argon requires intensive and continuous maintenance.

### 3.2 Magnetic sector field deflection

The ion beam deflection through the magnetic sector field in the dipole magnet was characterized with the current measurement at the target. Once a stable 6 kV deuterium ion beam had been achieved, the beam-stopper was retracted and the strength of the magnetic sector field was slowly increased, while the current at the target was measured with an ORTEC 439 Digital Current Integrator. When using deuterium, three discrete, strong peaks were observed, corresponding respectively to the three ion species  $D^+$ ,  $D_2^+$  and  $D_3^+$ . The same test was repeated with a 6 kV hydrogen beam and a 6 kV hydrogen-helium beam from a mixed plasma with a 7:3 H-to-He flow ratio. The deuterium, hydrogen and hydrogen-helium peaks are shown in fig. 27. Again, three relatively large peaks were observed when using only hydrogen, corresponding to  $H^+$ ,  $H_2^+$  and  $H_3^+$ , respectively. Three small additional peaks are observed near magnet currents of 10, 12 and 20 A for deuterium and 7, 9 and 15 A for hydrogen. These are due, in the case of hydrogen, to  $H_2^+$  and  $H_3^+$  ions dissociating in-flight between the ion source and the dipole magnet into a neutral molecule or atom and an ion. The ion will continue its flight with a fraction of the rigidity (eq. 6) of the initial molecule, consequently achieving the same deflection in the magnetic sector field at lower magnetic field strengths, and thus lower currents through the dipole magnet. In this case, the 7 A peak corresponds to  $H_3^+$  ions separating into  $H^+$  ions with one third of the initial rigidity. This can be confirmed by applying equation 6 with constant gyroradius, showing that a peak at one third of the magnetic field strength is expected, which neglecting hysteresis and saturation effects corresponds to one third of the current for the  $H_3^+$  peak (eq. 7). If the  $H_3^+$  ion separates into a  $H_2^+$  ion and a neutral H atom, the ion retains two thirds of the initial rigidity and the peak is expected to be found at a magnetic field strength that is two thirds that of the  $H_3^+$  peak. Similarly, the 9 A peak corresponds to  $H_2^+$  ions separating into a neutral H and a  $H^+$  ion, retaining each half the rigidity of the original molecular ion. The neutral particle will not be deflected by the magnetic field. If helium is added to the gas mixture, a new  $He^+$  peak is observed in addition to the previous hydrogen peaks, shown in red in figure 27 at 24.7 A. A very weak additional peak was observed at a magnet current of approximately 28 A. It is believed this small peak corresponds to trace amounts of  $HeH^+$  ions [14].

If argon is used in the ion source,  $ArH^+$  is also produced. This ion, with molecular mass 41, is the dominant ion species under a wide range of operating parameters [15]. Consequently, a peak may be observed in the current measurement which can be hard to separate from the  $Ar^+$  peak of mass 40. For this reason, it is advised to admix the argon gas with deuterium instead of hydrogen in the ion source, since in this case  $ArD^+$  will be produced, with molecular mass 42. Since the rigidity difference between the two ions is in this case larger, the two peaks in the ion current measurement are distinguished more easily.

The dipole magnet was also tested in the same way with a Faraday cup mounted on the opposite exit (PERMEX exit in fig. 11). The polarity of the current through the electromagnets, i.e., the B-field, was flipped in order to deflect ions in the other direction. The sets of peaks observed were identical, regardless of the direction of the deflection. This proves the symmetric behavior of the magnet.

These tests were also repeated at differing ion energies. Figure 28 shows the rigidity of each ion, plotted as a function of the magnet current (which is proportional to the B-field) at which the corresponding peaks in the ion current measurement were observed. Hydrogen and helium ions with an energy of 6 keV are shown, as are deuterium ions at energies of 1, 3, 6 and 9 keV. As described in eq. 6, the rigidity of the ions scales linearly with the magnetic field at a given bending radius. In cases where the rigidity of the ions is approximately the same, for instance for 1 keV  $D_3^+$  ions, 3 keV  $D^+$  ions and 6 keV  $H^+$  ions, it can be seen that the dipole magnet currents at which those peaks occur also coincide. It must be noted that the extrapolated linear regression from the data does not pass through the origin, as would be expected from the equation. This is believed to be due to the hysteresis of the dipole magnet: when magnetized from a zero-field value, the iron follows a non-linear magnetization curve. The magnetic field strength “lags behind” the current through the dipole magnet.

### 3.3 Beam emittance and ion optics

In order to maximize the ion flux density arriving at the target, it was necessary to study and characterize the optical properties of the ion beam, as this would determine the final selection and placement of the ion lenses to be used. As a first step, the optical beam paths of the ions were calculated using the transfer matrix method, as, e.g., described in [13, 16]. This method ignores beam divergence due to space-charge effects and is based on the assumption of ideal beam emittance (i.e., emittance ellipse has zero area), but it is nevertheless useful as

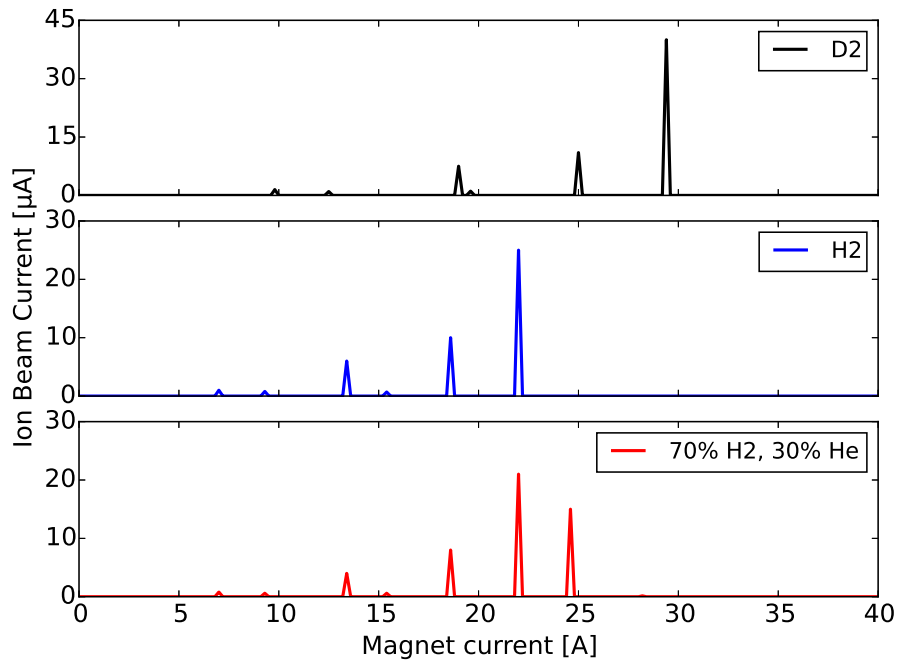


Figure 27: Ion currents from a 6 keV deuterium, 6 keV hydrogen and a 6 keV hydrogen (70% flow) and helium (30% flow) beam measured at the target chamber beyond the dipole magnet, as a function of the dipole magnet current, which is proportional to the magnetic field. In the upper plot, the peaks occurring in a pure deuterium beam are shown, with the three largest peaks corresponding to  $D^+$ ,  $D_2^+$  and  $D_3^+$ , respectively. In the middle plot, the respective  $H^+$ ,  $H_2^+$  and  $H_3^+$  peaks corresponding to a pure hydrogen beam are shown. In the case of a 70% hydrogen and 30% helium beam, shown in the lower plot, in addition to the hydrogen peaks, a peak corresponding to  $He^+$  is observed. The three smaller peaks occurring at magnet currents of approximately 10, 12 and 20 A in the case of deuterium and 7, 9 and 15 A for hydrogen correspond to ions that dissociate before reaching the dipole magnet, resulting in ion populations with lower rigidity. A very small peak at a magnet current of approximately 28 A is believed to correspond to a relatively small percentage of  $HeH^+$  ions [14].

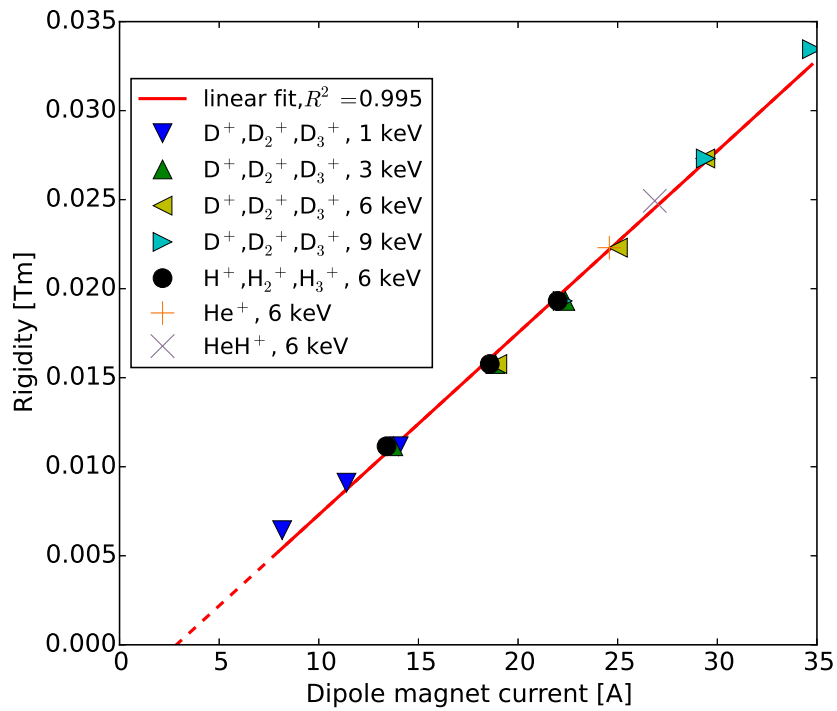


Figure 28: The rigidity of several ion species at energies ranging from 1 to 9 keV are plotted relative to the current applied to the dipole magnet at which the corresponding ion current peaks were measured. As predicted by equation 7, the rigidity is directly proportional to the current through the magnet, which is proportional to the magnetic field. It can be observed that ions whose mass times energy are identical coincide on the graph, such as 1 keV  $D_3^+$ , 3 keV  $D^+$  and 6 keV  $H^+$  ions. In discrepancy to the equation, the linear regression of the data does not connect to the origin. This is attributed to the magnet hysteresis. (Color online).

### Transfer matrix calculation of the ion optics between Mo aperture and target with two einzel lenses

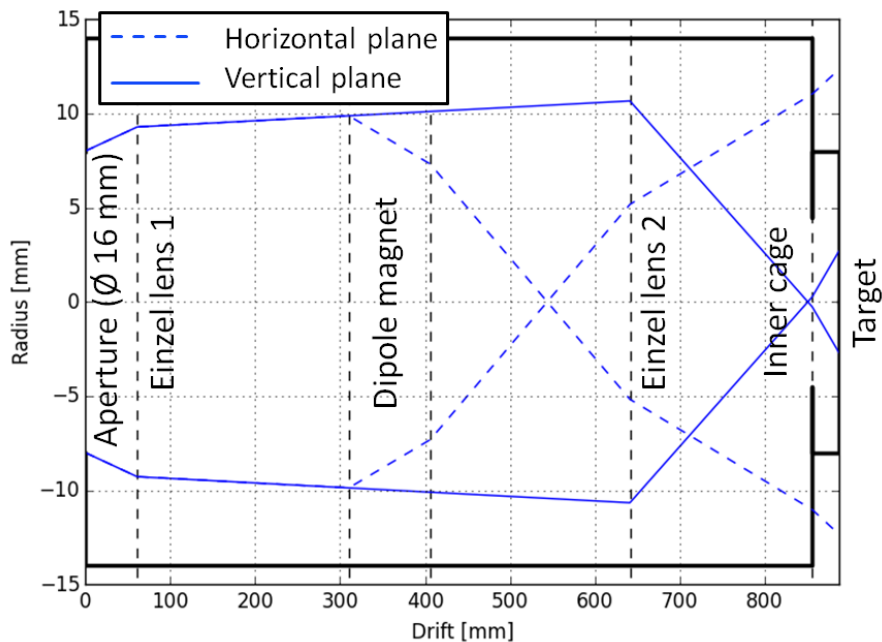


Figure 29: Calculation of the ion beam path by the transfer matrix method [16, 13] between the  $\text{\O} 16$  mm molybdenum aperture and the target, passing through two einzel lenses and the dipole magnet. Due to the magnetic focusing effect in the horizontal plane (dashed blue lines in the diagram), the beam is no longer cylindrically symmetric after passing through the dipole magnet. For this reason, the lens located after the magnet (“Einzel lens 2”) cannot focus the beam in both planes simultaneously, leading to a large part of the beam being lost [17].

a first-order approximation. Figure 29 shows the ion trajectories calculated by transfer matrices between the  $\text{\O} 16$  mm Mo aperture at the exit of the differential pumping stage and the target through the dipole magnet, with the addition of two einzel lenses, one at the position of the beam-stopper (i.e., directly in front of the entrance to the dipole magnet) and one before reaching the target chamber [17]. As a consequence of the deflection, the dipole magnet focuses the beam in the deflection (horizontal) plane but not in the perpendicular (vertical) plane. As a result, even in the case of initial cylindrical symmetry, the trajectories in the horizontal and vertical planes are not identical. Since einzel lenses are cylindrically symmetric, they cannot focus the beam onto the target simultaneously in both planes, leading to strong beam divergence and significant beam losses as a substantial part of the beam impinges on the apertures and walls of the vacuum tubes (e.g., entrance and exit tubes of the dipole magnet) and does not reach the target. The einzel lenses were also simulated with the open-source ion optics library IBSimu, which has been used in the past to simulate ion optics of lenses and ion sources [10, 18]. Fig. 30 shows an einzel lens that was used in the HSQ alongside a simulation of a similar lens without considering space-charge effects.

As previously stated, the beam at the differential pumping stage and beyond is strongly space-charge compensated: the thermal electrons trapped in the potential well of the ion beam neutralize the beam, strongly reducing beam divergence due to Coulomb repulsion [19]. The use of electrostatic einzel lenses thus intrinsically entails a trade-off: in order to effectively focus the beam, (at least) the central electrode must be set to a positive or negative potential typically of the same order of magnitude as the extraction potential of the beam. Electrons trapped in the ion beam will be repelled by or attracted to this electrode, leaving the beam and eliminating the space-charge compensation effect. As a consequence of this, the beam emittance would increase, potentially worsening beam transport, since the resulting space-charge would cause the ion beam to diverge significantly.

To test beam focusing and loss of space-charge compensation, two einzel lenses were installed: one located in the differential pumping stage at the exit of the ion source, shown in figure 31, and one located between the Mo aperture and dipole magnet. Due to space constraints, the beam-stopper had to be removed to install the second lens. The location of both lenses is shown in figure 1. The lenses were tested by applying decelerating (positive) and accelerating (negative) potentials to the central electrode of the lens with deuterium beams of 1.5, 3 and 6 keV. The ion current was measured with the Faraday cup at the beam-stopper in the case of the lens in the differential pumping stage and, due to the removal of the beam-stopper for the installation of the second lens, at a Faraday cup at the exit of the dipole magnet in the case of the lens mounted between the Mo aperture and the beam-stopper. Both lenses showed the same behavior, displayed in fig. 32 for the lens in the differential

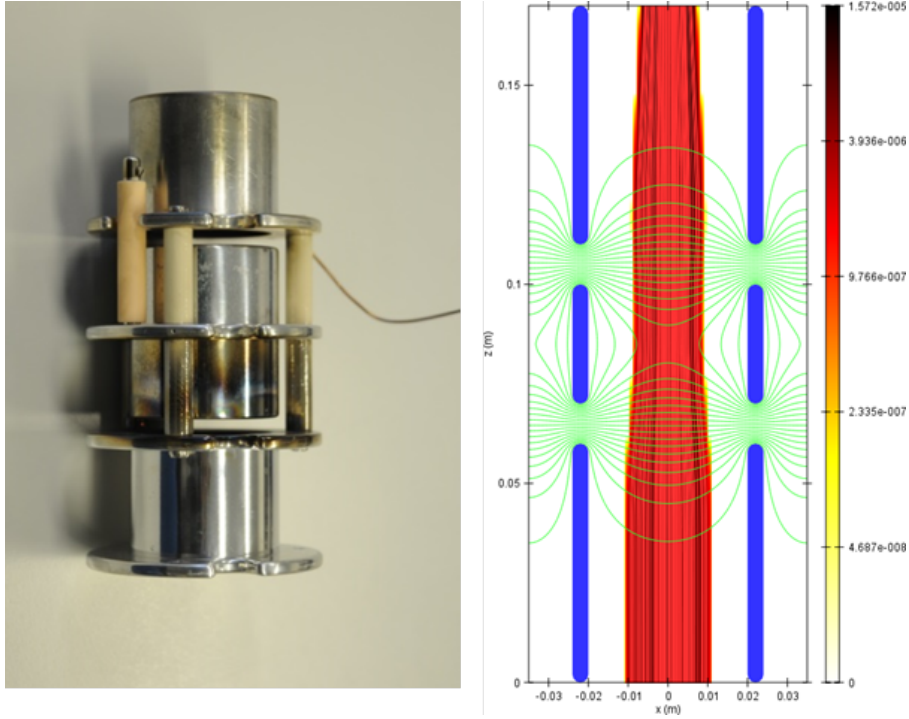


Figure 30: Einzel lens and ion optics simulation of a lens with IBSimu. In this simulation, the central electrode is set to a decelerating potential of +100 V while the first and third electrodes are grounded. A 5 mA beam with an extraction potential of +6 kV was used in this simulation. The lens on the left does not have the same geometry as the simulated lens and is only included for visualization.

pumping stage. In all cases, once a modest potential was set on the central electrode the measured ion current rapidly dropped by an order of magnitude. This is due to the loss of space-charge compensation. The effect was more pronounced when the einzel lens was set to a positive potential, since in this case the electrons were attracted towards the lens. When the lens was set to a negative potential, electrons were repelled by the lens. In this case, a significant decrease of the ion current occurred only for larger negative lens potentials, since space-charge compensation was only lost in the vicinity of the lens. The lens potential at which a significant decrease of the ion current is observed is proportional to the energy of the beam. As described in [16], a focus optimum occurs in all cases when operating the lens with positive polarity, at a potential slightly below and proportional to the extraction potential of the beam. This was evidenced by an increase in the measured ion current reaching the Faraday cup when setting the lens to the required potential. If the lens voltage is larger than the extraction potential of the beam, the ions are decelerated, and so the measured ion current drops to zero. This does not occur if the lens is operated at negative polarity because in this case the beam is accelerated towards the lens. If operated in this way, a more negative lens potential leads to stronger beam focusing, as evidenced by the slow increase in the measured current with negative lens potential. In all cases where the ion lenses were used, the ion currents that were measured were smaller than those measured when no lens was employed. The increase in focusing power does not outweigh the current losses due to emittance growth from space-charge.

The ion optical characteristics of the beam (beam profile and divergence) were studied at the exit of the dipole magnet. To visualize the beam, a Heraeus M-382 Plus<sup>17</sup> Ce-doped quartz glass was installed at a distance of 16 cm from the dipole magnet's exit flange. When ions impinge on the glass, light is emitted due to fluorescence. In order to avoid charge accumulation on the surface of the glass, a fine nickel mesh was attached to the glass with Kapton<sup>18</sup> tape. At the Mo aperture, the beam diverges equally in the horizontal and vertical plane and has a diameter of 16 mm. As can be seen in fig. 33, the focusing of the beam in the horizontal plane within the magnetic sector field leads to an elongated beam at the exit of the dipole magnet, with a narrow beam diameter of approximately 10 mm. In the vertical plane, the beam is not focused and the beam diameter is 34 mm. The real focusing effect at the position of the quartz glass in the horizontal plane is, therefore, from a diameter of 34 mm to one of 10 mm. At positions further downstream from the dipole magnet, the beam waist in the horizontal plane is reached and the beam again diverges in the horizontal plane. At the target, the beam divergence (and beam diameter) is larger in the horizontal plane than in the vertical plane. As previously stated, this beam astigmatism cannot be corrected with cylindrically symmetric lenses. Instead,

<sup>17</sup>Trademark of Heraeus Quarzglas GmbH & Co. KG

<sup>18</sup>Trademark of E. I. du Pont de Nemours & Co.

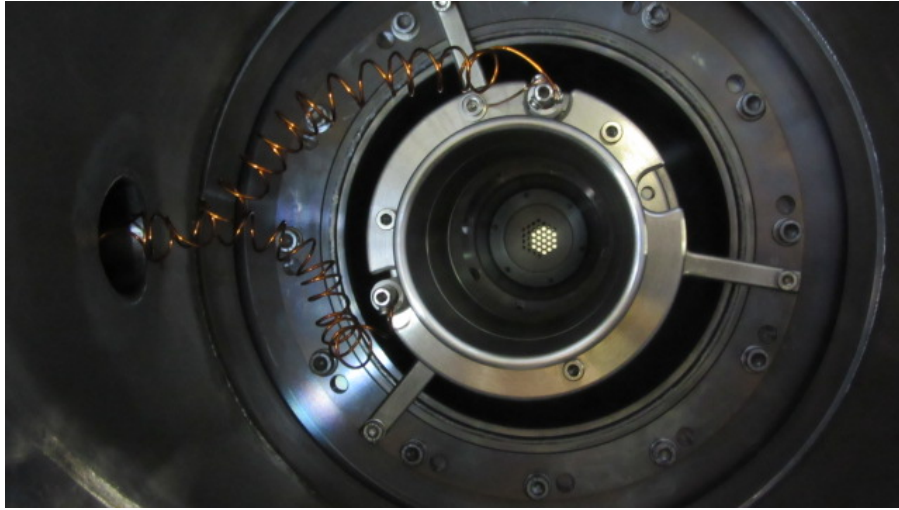


Figure 31: Einzel lens installed in the first differential pumping stage at the exit of the ion source, marked 1st einzel lens in the bird's-eye view of SIESTA (fig. 1).

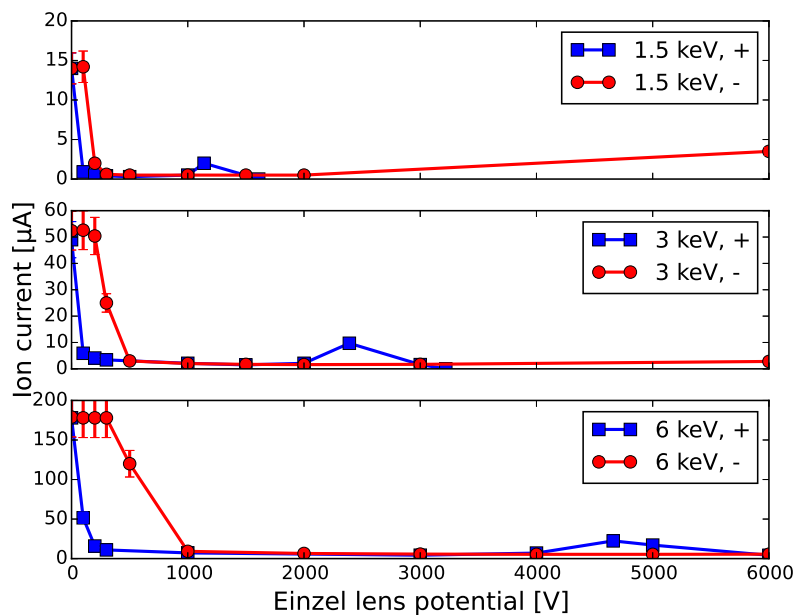


Figure 32: Ion currents measured at the beam-stopper from D beams of 1.5, 3 and 6 keV when operating an einzel lens at the exit of the ion source at varying accelerating and decelerating potentials. Space-charge compensation was lost after applying a modest potential to the lens, as evidenced by the rapid drop in the measured ion current. In no case were ion currents achieved that were larger than without a lens. Lines have been added to guide the eye.

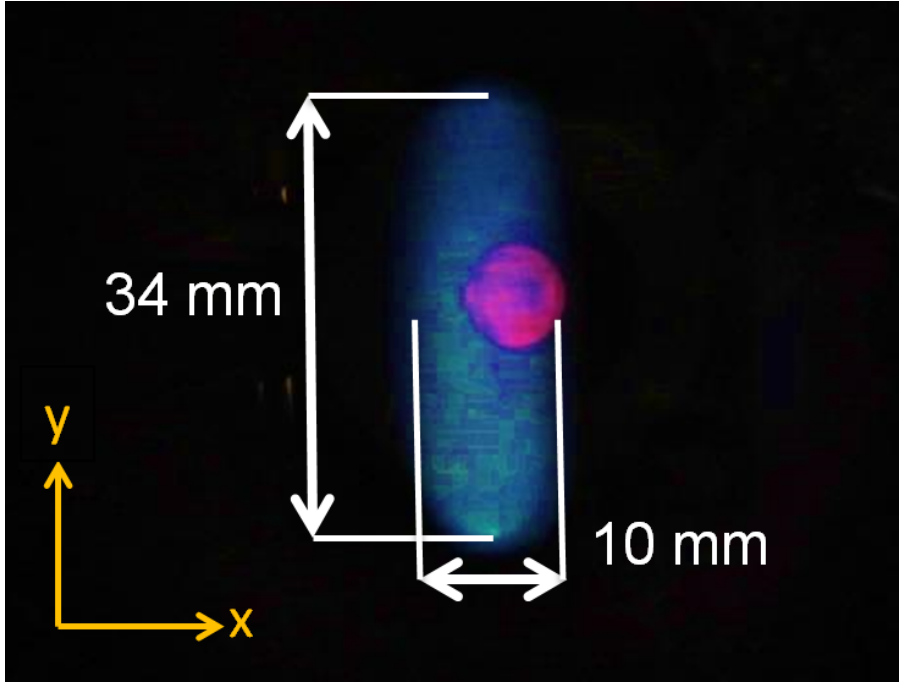


Figure 33: Beam profile of a 10 keV  $D_3^+$  beam on Ce-doped quartz glass 16 cm away from the exit of the dipole magnet. The beam is focused within the magnet in the deflection plane ( $x$ ), leading to an astigmatic beam with a beam-waist smaller than 10 mm at the quartz glass. The red spot in the middle of the image is light from the ion source that is reflected inside the dipole magnet, and bears no relation to the beam spot.

Parameter	Horizontal	Vertical
$\alpha$	3.7	-4.8
$\beta$	440	4400
$\gamma$	0.033	0.0054
$\epsilon$	0.28	0.056

Table 3: Twiss parameters in the horizontal and vertical planes at the exit of the dipole magnet

asymmetric lenses such as quadrupole lenses, capable of applying different foci in the horizontal and vertical plane, must be used. Since the loss of space-charge compensation incurs in significant beam losses, magnetic lenses - which will not attract / repel the electrons trapped in the beam - are preferred to electrostatic lenses. At a given position  $z$  along the trajectory of the beam, the angular distribution of the particle trajectories along a transverse direction  $x$  can be plotted, forming an ellipse in the  $(x, x')$  coordinate system, with  $x'$  denoting the angle of the beamlet in the  $xz$  plane (fig. 34). The emittance of a beam is the area of the ellipse divided by  $\pi$ , symbolized  $\epsilon$ . The ellipse parameters are denoted as  $(\alpha, \beta, \gamma)$ . Together with the emittance they are also known as the Twiss parameters [20]. As the particles continue on their trajectory, the shape of the ellipse is altered but the emittance remains constant.

The emittance ellipse was measured by the pepper-pot method, as described in [21, 22]. A plate with equally spaced holes (pepper-pot) was placed at the exit flange of the dipole magnet. As the beam passed through the holes, the beamlets produced individual beam footprints on the quartz glass. With this information, the angular distribution of the beam at the position of each hole on the pepper pot was measured, from which the beam ellipse is reconstructed to obtain the Twiss parameters [20]. Figure 35 shows the reconstructed ellipse in the horizontal and vertical planes along with the values of the Twiss parameters at the exit flange of the dipole magnet, also listed in table 3.

The measured Twiss parameters were used in ion optical calculations to design the magnetic quadrupole doublet lens. The magnetic fields of the quadrupole doublet were optimized in order to maximize the ion flux at the target. A single quadrupole focuses the beam in one plane while simultaneously de-focusing in the perpendicular plane. The horizontal and vertical focal points are, therefore, not independent. A combination of two allows for an additional degree of freedom, so that both focal points may be adjusted freely, and so net focusing in both planes can be achieved. Calculations showed the use of such a magnetic quadrupole could entail an increase of ion current at the target by up to a factor of 20 compared to values without installing the lens. Fig. 36 shows calculated trajectories of the edge of the beam in the horizontal and vertical plane between the dipole magnet and the target if a fully-optimized quadrupole doublet lens is used. Based on these results, a magnetic quadrupole doublet model QM-60.100 from D-Pace with a bore diameter of 60 mm and a peak pole-

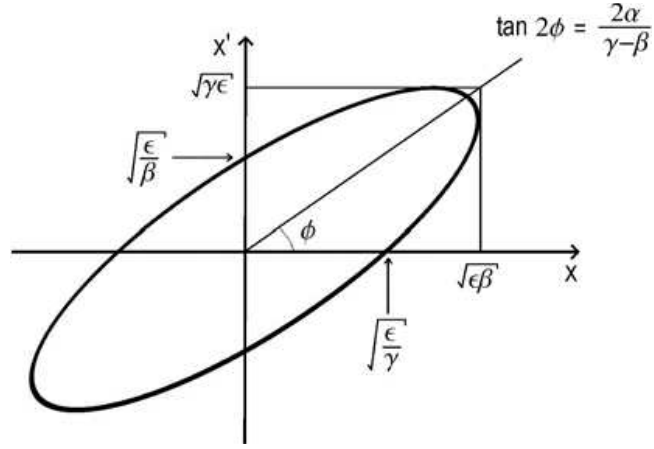


Figure 34: Emittance diagram showing the emittance ellipse parameters, also known as Twiss parameters. For a given position along a beam's trajectory  $z$ , the angular distribution of the trajectories along a direction transverse to the nominal path can be described by an ellipse in the  $(x, x')$  coordinate system where  $x$  denotes the distance along the transverse direction and  $x'$  denotes the angle of the beam with regards to  $z$  on the  $xz$  plane [20]

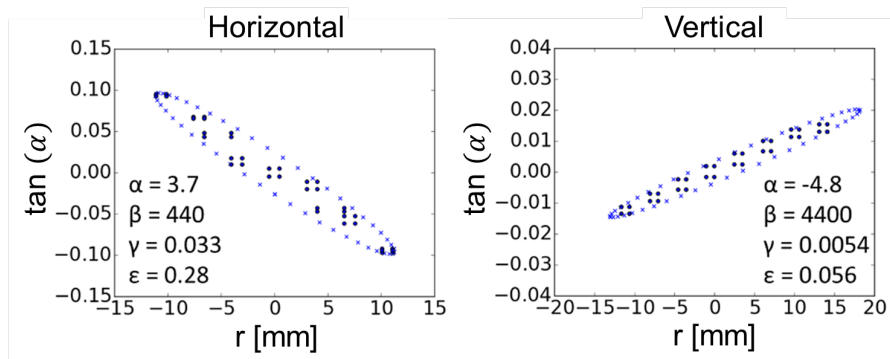


Figure 35: Reconstructed beam ellipses from a 10 keV  $D_3^+$  beam in the horizontal and vertical planes at the exit flange of the dipole magnet with the calculated Twiss parameters. Dark blue dots correspond to the measured points. Light blue crosses indicate the circumscribing ellipse. The beam is converging in the horizontal plane (negative angles for positive distances), while diverging in the vertical plane (positive angles at positive distances). The area of the ellipse is  $\varepsilon \cdot \pi$  in mm·rad.

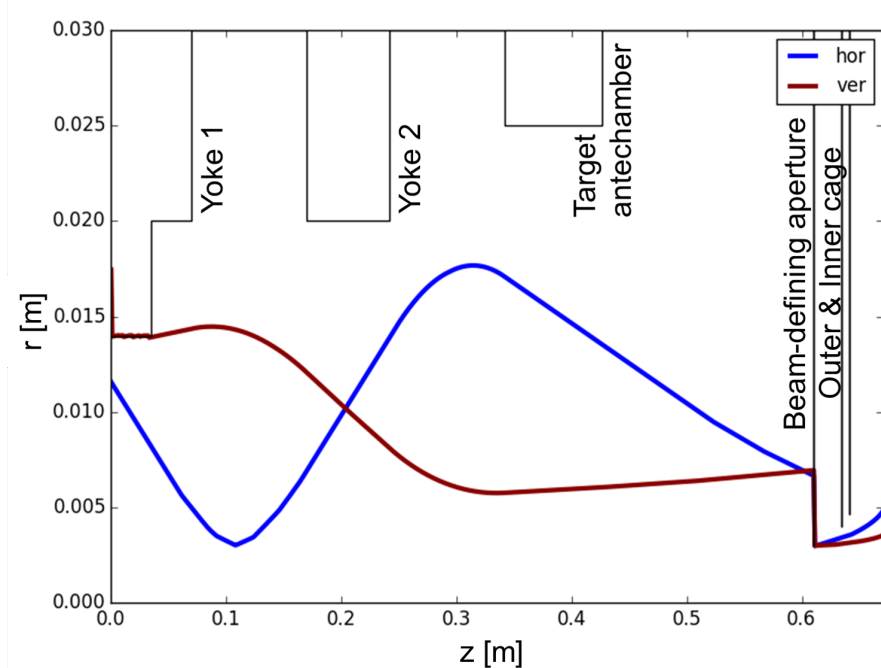


Figure 36: Numerical calculations of the edge of the beam trajectory through a magnetic quadrupole doublet between the dipole magnet ( $z = 0$  m) and the target ( $z = 0.6$  m) in the horizontal (hor) and vertical planes (ver) when focusing a 6 keV  $D_3^+$  beam. Between the grounded inner cage and the target (right edge of the image), the ions are decelerated to an impinging ion energy of 600 eV/D. The first quadrupole along the  $z$  axis focuses vertically with a pole tip field of 0.041 T and the second focuses horizontally with a pole tip field of 0.073 T.

tip field of 0.15 T was ordered and installed (quadrupole shown in fig. 12). The quadrupole doublet is situated outside of the vacuum system. The position of the quadrupole lens system is shown in fig. 1. As is visible in fig. 36, the beam trajectories may expand significantly within the quadrupole lens during focusing. In order to prevent contact with the walls of the vacuum tube connecting the dipole magnet and the target chamber under a wide range of possible operating conditions, the 321 mm long vacuum tube used to connect the two systems was custom built to have a larger internal diameter ( $\varnothing$  49.8 mm instead of the nominal  $\varnothing$  38 mm for a CF40 tube). In agreement with the simulations, the highest current at the target chamber was measured when the quadrupole closest to the dipole magnet was configured to vertically focus the beam and the quadrupole closest to the target chamber focused the beam horizontally. The position of the quadrupoles along the beam axis was varied by  $\pm 40$  mm from their nominal position. Experimentally, this was not seen to have any significant effect on the maximum ion current measured at the target chamber.

When focusing a 6 kV  $D_3^+$  ion beam with the quadrupole doublet lens, an increase of a factor of 4 in the ion current was achieved. The discrepancy between this and the factor of 20 increase predicted by the calculations is attributed to two factors. Firstly, the ion density of the beam was assumed to be uniform in the simulations and under this assumption, when no quadrupole lens is used, a large part of the ion current would impinge on the stainless steel walls of the vacuum chambers and the beam-defining aperture. If the ion density is not uniform, but instead higher near the center of the beam, then a larger fraction of the beam would reach the target without the use of a lens, in which case the possible increase in ion current at the target due to the addition of said lens would be smaller than predicted. Secondly, the focusing effect of the quadrupole lens is highly sensitive to the correct alignment of each of the two quadrupoles. It was observed that a sub-mm precision is required to adequately focus the beam. This was not foreseen when designing the support structure for the quadrupole doublet lens, and it is possible that the lens is not yet sufficiently well aligned with the target. If this is the case, then better alignment may provide larger ion currents at the target. In view of this, a fine-adjustment support structure is to be installed in the future.

### 3.4 Beam footprint and neutral population at the target

The beam footprint at the target was measured without focusing from the quadrupole lens by exposing samples consisting of a 70-nm-thick layer of amorphous hydrogenated carbon (a-C:H) on a Si substrate to a deuterium ion beam. For these samples, a change in layer thickness of a few nanometers leads to a change in color. This change in layer thickness was quantitatively measured applying ellipsometry [23]. Two a-C:H samples were eroded by a 6 keV  $D_3^+$  beam when using a  $\varnothing$  6 mm beam-defining aperture. Figure 37 shows the 2D-ellipsometry measurements and horizontal line scans of the samples, from which 20 nm on average were eroded

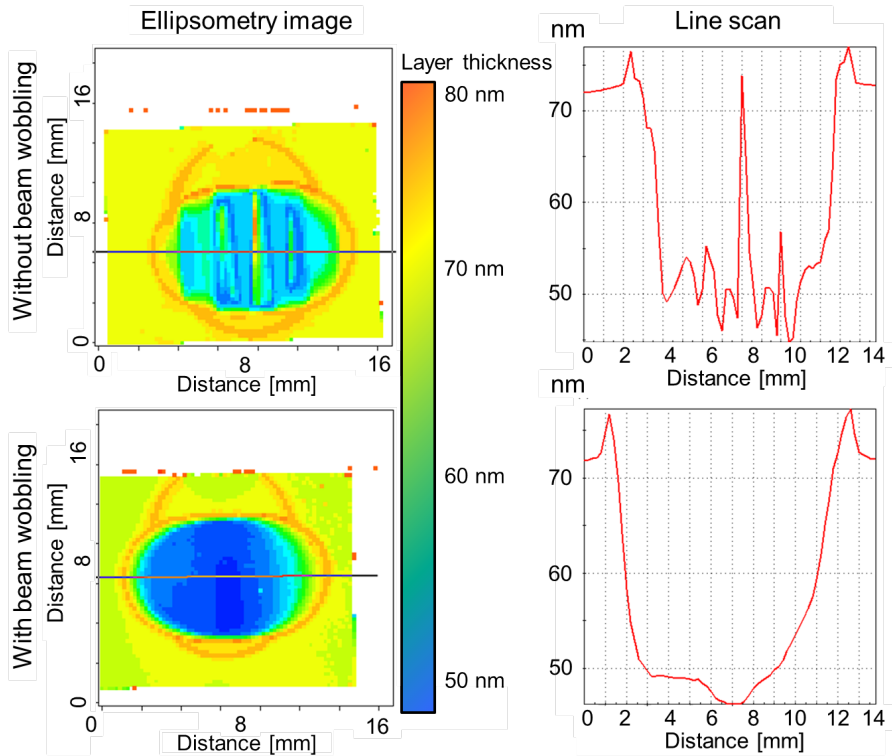


Figure 37: Ellipsometry measurements of the beam footprint at the target obtained by exposing a 70-nm-thick a-C:H layer on Si of a 6 keV  $D_3^+$  beam, when using a  $\varnothing$  6 mm beam-defining aperture. The images on the left show a 2D pattern of the a-C:H layer erosion. The images on the right are line scans along the line indicated in the left figure. In the lower pair of images, the ion beam was scanned over the beam-defining aperture. For details please refer to the text. (Color online). [23].

in each case. On both samples, the ion beam footprint corresponds to the horizontally-elongated ellipse. Since the beam diverges differently in the horizontal and vertical planes between the beam-defining aperture and the target (stronger divergence at the target in the horizontal plane), the footprint of the beam is elliptical and the surface area of the beam-defining aperture cannot be taken as the surface area of the beam footprint. A second vertically elongated ellipse is also visible on the sample. This ellipse is assumed to be caused by a small percentage of neutral particles which impinge on the a-C:H layer, altering the optical properties of the surface. The neutral population of the ion beam is quantified at the end of this section.

In the topmost image, evenly-spaced vertical lines are visible along the horizontal axis of the sample. This is due to areas with different erosion. These vertical lines, of approximately 1 mm in width, are a consequence of the horizontal beam focusing effect of the dipole magnet: after passing through the magnetic sector field the beam is focused in the deflection (horizontal) plane, forming an image of the openings of the last (grounded) of the three grids (described in section 2.2) located at the exit of the ion source. The first and second grids are shown in figure 3. No image is formed in the vertical plane, because in this plane the focal point is not located upstream from the target chamber. Since the holes of the grids are vertically aligned, they appear as vertical stripes on the sample. Due to the construction of the grids, it is not possible to rotate them in a way that will eliminate the stripes. To accomplish this, new grids with an altered geometry would have to be manufactured. One way to avoid the formation of these vertical stripes is to periodically vary the current through the dipole magnet back and forth by a small amount, typically  $\pm 0.2$  A, thereby “sweeping” the ion beam over the beam-defining aperture. This was performed when eroding the second a-C:H sample (lower images of figure 37). The increase in layer thickness at the edge of the beam-spot visible in both images (orange) is an artifact of the ellipsometry measurement. D implantation into the a-C:H layer leads to a change of the optical properties of the layer, which are interpreted by the analysis software as an increase of the layer thickness [23].

When using the quadrupole doublet lens to focus the beam, similar inhomogeneities in the beam footprint at the target are also observed, although depending on the lens focusing effect, these may not necessarily take the shape of vertically elongated lines. As was the case without focusing with the quadrupole lens, oscillating the current through the dipole magnet to sweep the beam over the beam-defining aperture also helps to “smooth out” the inhomogeneities in the beam-footprint at the target. Another alternative to reduce said inhomogeneities would be to induce vertical and horizontal beam-sweeping by operating each of the four coils of the quadrupoles separately. However, this method would compromise the beam focusing effect of the quadrupole lens which is responsible for the increase in ion flux to the target. Since this was the main application of the quadrupole lens,

Angle [°]	Surface Area [cm <sup>2</sup> ]	Aperture [mm]
0	0.51	Ø 6
45	0.75	3 x 6
60	0.82	2 x 6
75	0.94	1.5 x 6

Table 4: Measured surface area of beam footprint on a-C:H samples eroded under varying angles of incidence by a 6 keV  $D_3^+$  beam. The required aperture was chosen for each angle to ensure the beam only impinged on the sample.

this method to homogenize the beam footprint was not attempted. Electrostatic beam-sweeping with capacitor plates was also not implemented, as this would have led to a loss of space-charge compensation in the ion beam, as was evidenced in the tests with einzel-lenses in section 3.3.

Samples coated with a-C:H layers were also used to measure the surface area of the beam footprint at the target, which is required together with the impinging ion current to calculate the ion flux density (and fluence) at the target. Table 4 shows the measured surface areas eroded by a 6 keV  $D_3^+$  beam under various angles of incidence. To prevent part of the beam from extending beyond the target and impinging on the inside of the double cage, the appropriate beam-defining aperture had to be chosen for each angle of incidence at which a measurement took place.

Ions can be neutralized in-flight in between the ion source and the target by charge exchange collisions. Neutral particles produced between ion source and dipole magnet will not be deflected and, therefore, will not reach the target. If experiments with low-energy ions are desired, the target will be biased to decelerate the ions. However, high energy neutral particles produced between the exit of the dipole magnet and the target double cage will not be decelerated and may impinge on the target with the full primary energy. Given the difference in impinging energy, the effect of these impinging neutral particles on the sample can, in some cases, be of comparable magnitude to the effect of the much higher flux of low-energy ions. Therefore, if the impinging neutral particles are not taken into account, this neglect can severely compromise the interpretation of the experimental results. In order to assess the impact of the neutral particles, the neutral population of the beam at the target was quantified. As a first step, the neutral population was estimated analytically by equating the neutral population with the probability of neutralization  $P$ , which is taken as a first approximation as:

$$P = \sigma nL, \quad (8)$$

where  $\sigma$  is the charge exchange cross section. No charge exchange cross section data could be found for  $[D_3^+, D_2]$ , but as a first approximation the cross section is assumed to be similar to that of  $[D^+, D_2]$ , which for 3 keV  $[D^+, D_2]$  is  $2 \times 10^{-19} \text{ m}^2$ , taken for  $H$  from [24] with the corresponding energy correction. The density of neutral gas between dipole magnet,  $n$ , is derived from the gas pressure by applying the ideal gas law at room temperature. As a conservative assumption, the neutral gas density was calculated with the pressure in the dipole magnet ( $5 \times 10^{-6} \text{ mbar}$ ), which is higher than the pressure in the target chamber ( $5 \times 10^{-7} \text{ mbar}$ ), leading to  $n = 1.2 \times 10^{17} \text{ D}_2/\text{m}^3$ .  $L$  is the distance between dipole magnet and target, which in the case of SIESTA is 0.6 m. By applying equation 8, the neutral population is estimated as 1.4%.

To measure the neutral fraction in the beam a thin gold layer on a silicon substrate was exposed to a D ion beam. Physical Vapor deposition was used to produce a sample consisting of a 45 nm Au layer on a smooth Si substrate, with a 5 nm Ti interlayer included to ensure adequate adhesion of the Au layer and to act as a diffusion barrier between Au and Si. The 2-dimensional thickness distribution of the Au layer was measured by Rutherford Backscattering Spectrometry (RBS) with 2 MeV  $He^+$  ions with an analysis beam-spot size of approximately  $1 \times 1 \text{ mm}^2$ . The maximum variation of the thus-determined Au-layer thickness across the surface of the sample was 0.5 nm, indicating the very good homogeneity of the Au layer. The sample was subsequently exposed at SIESTA to a neutral deuterium beam of 1.2 keV/D by employing an extraction potential of 3.6 kV to extract  $D_3^+$  ions and positively biasing the target to 3.8 kV. By biasing the target in this fashion, all deuterium ions are deflected away from the target and do not reach the sample, while the fraction of neutral particles in the beam is not affected by target biasing and thus impinges with full extraction energy on the sample. The sample was exposed in this manner for 32 hours. During this exposure, the  $D_3^+$  ion current was measured periodically by rotating the target platform  $180^\circ$  and allowing the beam to impinge on the backside of the grounded heating cup, which as stated in section 2.6 is connected to the current measurement for this purpose. The current was determined to be constant, with a variation below 1% during exposures. The day to day variability of the current between exposures was registered and accounted for.

After erosion, the Au-layer thickness was again measured by RBS and the eroded Au-layer thickness was determined. Measurements were carried out in 1 mm steps along the longitudinal midplane of the sample and perpendicular to the midplane at the position of the measured erosion maximum. The measured beam spots

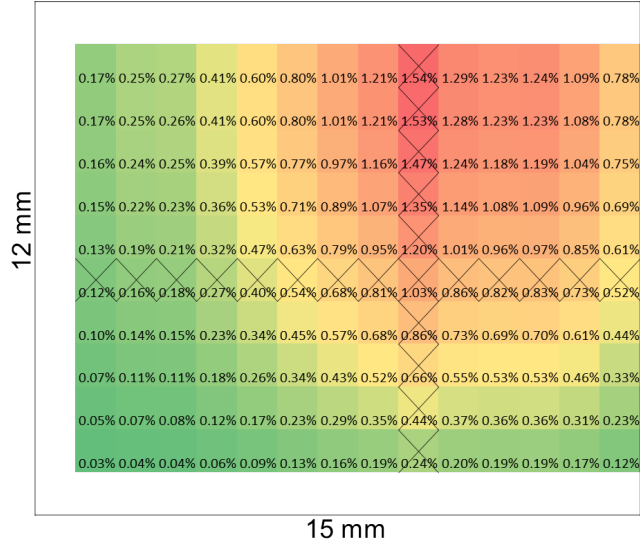


Figure 38: Position-resolved neutral population at the target measured on a 12x15 mm sample. The percentage in each cell represents the neutral population of the impinging beam on that 1x1 mm cell. Red corresponds to areas where the neutral population is larger than 1%. Yellow indicates it is between 0.5% and 1%. Green indicates the neutral population is below 0.5%. X marks the positions where the neutral population was measured by RBS. The neutral populations at all other positions were interpolated by the tensor product method from the measured data.

are marked with an X in fig. 38. The sputter yield for 1.2 keV/D on Au is 0.0305 and was taken from [4]. With this method, the neutral fluence at each of the positions measured with RBS was calculated. These data were contrasted with the exposure time and average ion current to determine the neutral population of the ion beam at said positions. The neutral population is calculated as the number of energetic neutral D atoms divided by the number of D atoms arriving in form of ions, i.e., in the case of  $D_3^+$  ions the latter number is three times the ion flux. The erosion - and thus neutral population - at other positions on the sample was interpolated from these measurements by applying the tensor-product method. The maximal measured thickness change was 41.7 nm corresponding to 93% of the 45-nm-thick Au layer. At its maximum, the neutral population is of 1.5%, while the average among the measurement points is of 0.8%. As shown in figure 38, the neutral beam is predominantly concentrated off-center on the upper-right quadrant of the sample. The beam footprint of the neutral “beam” differs from that of the ion beam under equivalent exposure conditions (i.e., if the target were not biased) because the ion beam would be focused by the quadrupole doublet lens, whereas in the case of the neutral “beam”, those ions neutralized between the exit of the dipole magnet and the first quadrupole (the majority, since the pressure in the dipole magnet is larger than in the target chamber) would not be focused at all. Those neutralized between the quadrupoles would be focused by the first one and not by the second one, and only those ions neutralized between the second quadrupole and the target would be focused in the same way as the ion beam. The neutral “beam” can be considered a combination of these three beams. Due to small errors in the adjustment of the quadrupoles (mentioned briefly at the end of section 3.3), the axes of the two quadrupoles and the exit of the dipole magnet do not completely coincide, so the overall neutral “beam” trajectory is slightly off-axis with regard to the ion beam.

The neutral population of the ion beam has been estimated to be approximately 1% under the given exposure conditions. Based on this information, e.g., in the case of sputtering at low incident ion energies, if the sputter yield of the high-energy neutrals is larger than the sputter yield of the low-energy ions by a factor of 100 or more, the neutral particles will substantially contribute to or even dominate the sputtering process, and therefore cannot be neglected. In such cases, it may be necessary to perform a dedicated measurement of the neutral population analogous to this one under the required experimental conditions.

### 3.5 Current measurement

The target high-voltage power supply was modified to avoid unintentional charging of the sample when this was irradiated by an ion beam. When this happened, the sample would accumulate charge if the power supply was set to positive polarity. At an ion current of 50  $\mu$ A, this would lead to an unintended sample bias of between 1 and 2 kV. When operating the power supply in this fashion, the diodes are opposing the flow of a “positive” (i.e. ion) current, so the sample charges up until arcing with another component occurs. To understand why this was

not an issue in the HSQ, the circuit schematics of the old Heinzinger HNCs 6000<sup>19</sup> power supply and the new FUG 430M-6000 were compared. It was found that a bridge with a 400 k $\Omega$  resistor between the high voltage pin (HV) and the 0 V pin was present in the Heinzinger power supply and absent in the FUG power supply. When using the Heinzinger power supply at positive polarity, the positive ion current would flow through the resistor to the 0 V pin, thereby preventing the target from charging up dramatically. It must be noted, however, that the flow of current does induce slight potential difference proportional to the resistance that is installed (in the case of 400 k $\Omega$  and 50  $\mu$ A, the potential will be  $U = R * I = 20$  V). If the target is set to a certain potential, current will also flow through the bridge, leading to an ohmic power loss inversely proportional to the installed resistance. If the bias is 6 kV,  $P = U * I = \frac{U^2}{R} = 90$  W.

Based on this, the FUG power supply was modified by the manufacturer to include a similar bridge with a 200 k $\Omega$  resistor, leading in the aforementioned cases to an additional bias of 10 V under an ion current of 50  $\mu$ A and leading to a power loss at 6 kV of 180 W. Thanks to this bridge, no additional charging of the sample has been observed.

The current measurement was tested under both connection scheme configurations (scheme A and scheme B, fig. 16), while varying the target bias and outer grid voltage, and was already described in section 2.6. If the target and outer grid are unbiased, the ion current is overestimated by the current measurement due to secondary electrons emitted at the target. If the outer grid is negatively biased, these secondary electrons are repelled by the outer grid and are collected at the inner grid, which is connected to the current measurement. Increasing the outer grid negative bias led to a decrease of the measured ion current up to a bias of -7 V, beyond which point the ion current was stable. As a precaution, a nominal negative bias at the outer cage of -10 V was chosen, as at this bias the current measurement is stable and the bias is well above the measured threshold of -7 V. If the outer grid was grounded, a positive bias set to the target also had an effect on the measured ion current (secondary electrons are retained, electrons trapped in the potential well of the beam are attracted). It was however observed that, once the negative bias of the outer cage was set to -10 V the bias at the target no longer played a role in the beam current measurement. As a precaution, it was decided that a positive bias of 100 V (or greater, if required to achieve lower ion energies) at the target should be used to retain any secondary electrons. The inner cage is kept grounded through the current measurement at all times (fig. 16).

The energy of the beam at the position of the target was checked by employing the target holder and heating cup as a retarding field analyzer. The ion current was measured only at the grounded heating cup located behind the target holder and a fine, optically thin Ni mesh (transparency 73%) was attached to the target holder instead of a sample. The target could be grounded or positively biased. All other components were grounded. When the target was grounded, the ion beam passed through the openings in the mesh unimpeded and reached the heating cup, where the current was measured. At low target biases, the beam was partly deflected, but part reached the heating cup, producing secondary electrons which were accelerated towards the target holder, leading to an increased current measured at the heating cup. The bias at the target holder was progressively increased until the measured current abruptly fell to zero. When this happened, the bias of the Ni mesh corresponded to the energy of the beam. The beam was completely deflected by the Ni mesh at the target holder and no ions were reaching the heating cup. With this method, the energy of a 3 keV beam was confirmed to within 30 eV.

### 3.6 In-situ weight loss measurement

As previously mentioned in section 2.6, a microbalance is installed above the target chamber, directly over the target platform, and is used for in-situ weight loss measurements. The balance is a Rubotherm LP-type<sup>20</sup> magnetic suspension balance with a maximum load of 20 g with  $\pm 1$   $\mu$ g nominal resolution.

The operating principle of the balance, depicted schematically in figure 39, is as follows: The balance including sensor coil and electromagnet is located outside of the vacuum system. A double-walled copper tube closed on its upper end is used as separation between the sample in the vacuum system and the balance. A measuring rod consisting of a permanent magnet and a measuring load coupling is located inside the copper tube and is secured with a deposit screw inside the vacuum system. The vertical position of the measuring rod is registered by the sensor coil and the current through the electromagnet can be regulated by the microbalance to elevate and suspend the permanent magnet. The load to be measured is attached to two hooks hanging from the measuring load coupling. If the rod is elevated sufficiently, the measuring load coupling with load is also lifted. The measuring rod with load is kept suspended at a fixed vertical position (measuring point) and the weight of the measuring rod with load can be determined from the current passing through the electromagnet. The measuring rod can be suspended at another fixed vertical position labeled zero point, which is lower than the measuring point. At this position, the load is not lifted and the balance may be calibrated and tared. In the case of SIESTA, the load (sample mounted on sample holder) is attached to the measuring hook by elevating and rotating the sample with the vertical manipulator on which the target platform is mounted.

<sup>19</sup>Trademark of Heinzinger electronic GmbH

<sup>20</sup>Trademark of Rubotherm GmbH

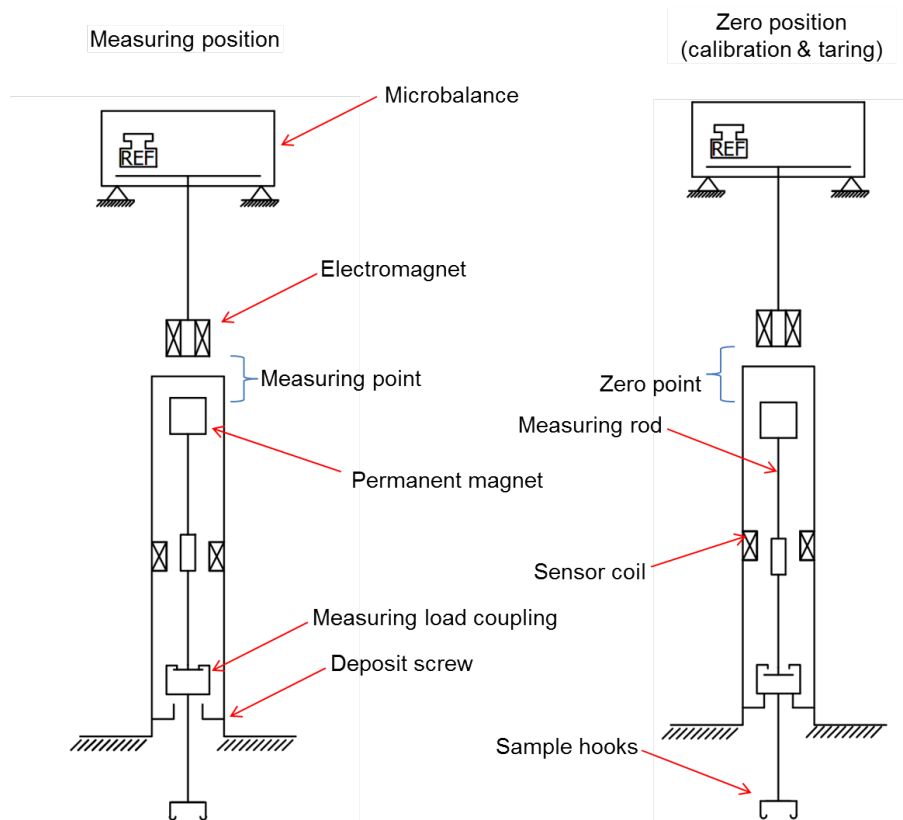


Figure 39: Measurement principle of the Rubotherm magnetic suspension balance. When set to “Zero” mode, the permanent magnet is suspended to the zero point (load not suspended) and the balance is tared and automatically calibrated. When in “Measuring” mode, the permanent magnet is suspended at the measuring point, lifting the sample.

The microbalance is highly sensitive to vibrations and electromagnetic fields. For this reason, the magnetic quadrupoles, dipole magnet and ion source power supplies must be switched off during measurement with the microbalance. To reduce transmission of vibrations from the vacuum pumps to the microbalance through the walls of the vacuum system, the microbalance is connected to the target chamber with a CF 40 bellows with a nominal length of 105 mm. Another CF 40 tube with a CF 40 viewport is also used to connect these two systems. Through this viewport the measuring load coupling, deposit cage and screw can be observed (shown in fig. 40). The microbalance is placed on top of an aluminum fine adjustment plate which allows lateral placement of the microbalance to within 0.1 mm. The fine adjustment plate is in turn located on top of a second Al plate connected to the target chamber support structure by rubber vibration dampers, serving to further insulate the microbalance from vibrations. To facilitate outgassing of the microbalance in the vacuum system, the double-walled copper tube was baked at 70°C for 10 days. Future improvements to the experimental setup could include thermal and magnetic shielding of the measuring head and sensor housing.

The microbalance control electronics is connected via an RS232 serial bus to a computer. Proprietary control software is used to operate the balance remotely and to carry out automated weight-measurement procedures. The general measurement procedure at SIESTA is as follows:

Once the sample is placed on the target platform via the load-lock horizontal manipulator, it is allowed to degas for 30 minutes. The sample is elevated and rotated so that the target holder upper hooks (visible in fig. 14 left and in fig. 15) are hooked on the microbalance measuring hook. Before weighing the sample, the microbalance is set to “Zero” position (diagram on the right in fig. 39) and is automatically calibrated and tared. The microbalance is subsequently set to “Measure” position and the sample weight is measured at 1 s intervals for 3 minutes. After this time the microbalance is once again set to “Zero” position, the drift in the weight measurement is corrected and the balance is once again tared. This “Measurement” and “Zero” cycle is repeated for 30 minutes.

By weighing the sample in this fashion before and after erosion, the mass loss of the sample due to erosion can be determined with a measurement uncertainty in the range of tens of  $\mu\text{g}$ . The microbalance was tested by comparing an in-situ weight loss measurement with an ex-situ measurement of the same sample. The experimental procedure and measured mass loss in these two cases are described at the end of section 4.

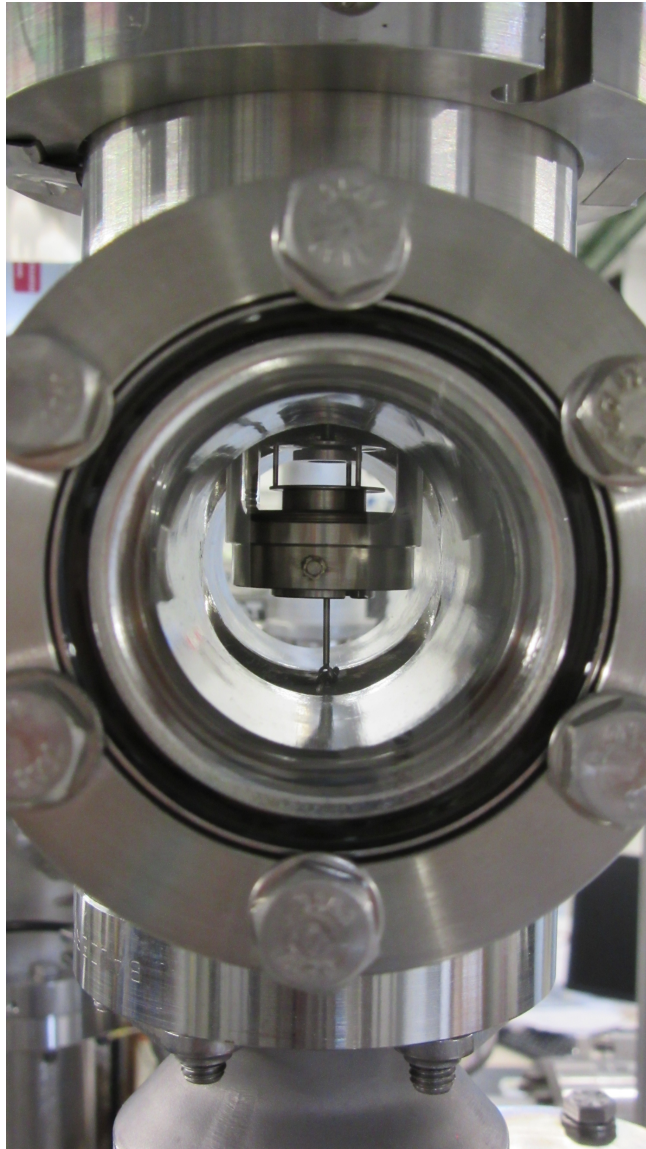


Figure 40: Microbalance measuring load coupling observed through CF40 viewport above the target chamber.

## 4 Erosion of Au bulk samples

### 4.1 Experimental procedure

Gold was chosen as target material for the characterization of SIESTA due to three material properties: firstly, due to the high molar mass of Au, significant weight loss can be achieved with moderate erosion. Secondly, the sputter yield (SY) of D on Au in the keV range is relatively high compared with that of its neighbors in the periodic table, so a comparatively lower fluence is required to achieve the desired erosion (e.g., SY of 2 keV D on Au is 0.037; SY of 2 keV D on W is 0.005 [3]). Thirdly, since Au is a noble metal, in-situ and ex-situ weight loss measurements can be directly compared without the need to consider the possible formation of an oxide layer.

Four pure gold bulk samples of 12x15 mm were mechanically polished to a mirror finish and were eroded by a 6 keV  $D_3^+$  ion beam (yielding 2 keV/D) at room temperature under normal incidence. All samples were weighed before and after exposure in an ex-situ microbalance. The sputter yield was determined by mass loss, and was compared to data from literature and simulations with the SDTrimSP code [25]. Said simulations were performed with the standard parameters (Gauss-Mehler quadrature integration method with 8 pivots and ipot set to 1).

To include the slight day-to-day variability in the operation of the ion source (slightly different pressure or gas flow in the source, source filament aging...), the samples were exposed on different days. On each day, the samples were weighed ex-situ in the morning, exposed during the day and weighed again after exposure in the evening. A reference sample was weighed alongside the exposed sample on each occasion to correct for potential drift in the linearity of the ex-situ microbalance measurement during the day due to environmental factors such as temperature or humidity. The samples were weighed several times on each occasion, with a 5-10 minute wait between measurements to allow the balance to stabilize. The balance was also tared between measurements. Additionally, one of the samples was weighed in-situ immediately before and after D ion beam exposure following the procedure described in section 3.6.

### 4.2 Sputter yield results

The sputter yield was calculated by applying:

$$SY = \frac{\Delta mass [g] \times N_A [\text{atoms/mol}]}{N_{ions} \times M(Au) [g/mol]} \quad (9)$$

Here  $\Delta mass$  is the mass loss due to erosion,  $N_A$  is Avogadro's number,  $M(Au)$  is the standard atomic weight of gold and  $N_{ions} = 3 \times Q [C] / e [C]$  is the total amount of impinging particles.  $Q$  is the collected charge at the target and  $e$  is the elementary charge.

The results are shown in figure 41. The average of the sputter yields obtained experimentally in this work is approximately 15% higher than the yield calculated by SDTrimSP, and approximately 25% higher than the average of the data points from literature [3, 26], though it must be noted that these show a significant scatter. The value given by SDTrimSP is within the scatter of Behrisch's data points [3] and shows good agreement with Bay [26]. It was decided to take the SDTrimSP value as the benchmark for SIESTA. Given that the experimental data points from SIESTA show comparatively low scatter (< 4%), it is unlikely that the deviation of 15% between the experimentally-obtained average and the SDTrimSP sputter yield is due to an issue with reproducibility at SIESTA. The deviation could possibly be attributed to a systematic error in the current measurement. Sputtering due to the presence of energetic neutral particles (explained and quantified in section 3.4) would also contribute to this error in measurement (though it would not be sufficient on its own to explain the discrepancy), as could a possible systematic error in the weight loss measurement.

In the case of the sample weighed in-situ and ex-situ (magenta diamonds in figure 41), the difference in the weight loss measurements is 20  $\mu g$  (759  $\mu g$  ex-situ versus 739  $\mu g$  in-situ). This is substantially larger than the standard deviation of the measurements, which in both cases is below 3  $\mu g$ . While this difference is statistically significant, the relative difference of the in-situ and ex-situ weight loss (and sputter yield) measurements is 2.6%, which is within the scatter observed in the ex-situ measurements. As such it can be stated that the in-situ microbalance is an adequate tool for determining the sputter yield through mass loss at SIESTA in this case, where the measured mass loss is large and therefore the relative error is small. However, further tests are needed to ensure its reproducibility under experimental conditions where the expected weight loss is smaller than 100  $\mu g$ . As stated in section 3.6, thermal and electromagnetic shielding may have to be installed to minimize the influence of external perturbations on the in-situ weight loss measurement.

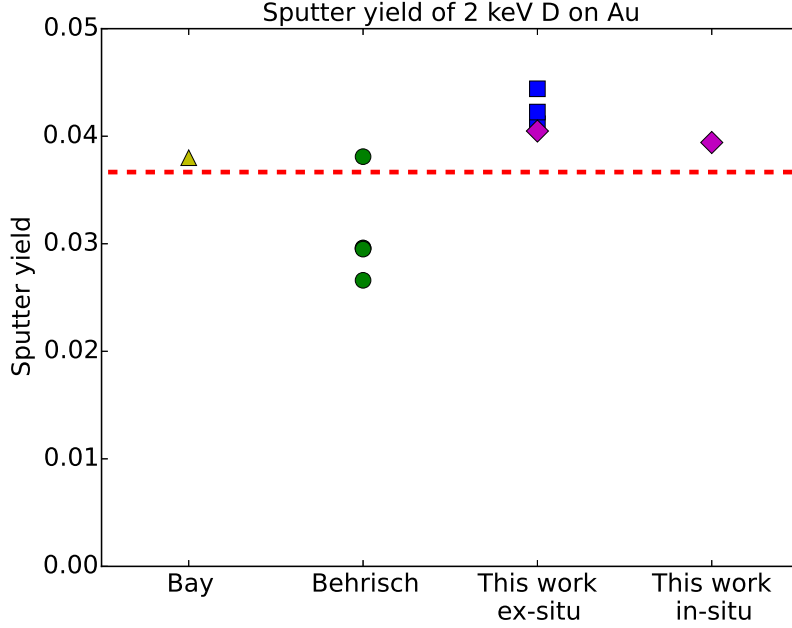


Figure 41: Sputter yield of bulk Au samples exposed to a 2 keV D beam ( $6 \text{ keV } D_3^+$ ) at SIESTA, determined by ex-situ and in-situ weight loss. In the case of the magenta diamonds, ex-situ and in-situ weight loss measurements were performed on the same sample. An SDTrimSP simulation and literature values from Behrisch [3] and Bay [26] are included for comparison. The uncertainty of the experimental sputter yield measurements (“This work ex-situ” and “This work in-situ”) is contained within the size of the symbols. (Color online).

Ion species	Energy at target [eV/atom]	Flux density [ $10^{19} \text{ atoms m}^{-2}\text{s}^{-1}$ ]	With quad. lens [ $10^{19} \text{ atoms m}^{-2}\text{s}^{-1}$ ]
$H^+$	6000	0.22	
$H_2^+$	3000	0.37	
$H_3^+$	2000	0.94	
$D^+$	6000	0.28	
$D_2^+$	3000	0.41	
$D_3^+$	2000	1.5	6.0
$D_3^+$	1000	1.3	
$D_3^+$	200	1.0	3.7
$He^+$	6000	0.45	
$Ar^+$	5000	0.10	0.37

Table 5: Performance data for SIESTA. Ion flux densities at the target are listed for varying ion species and energies at normal incidence. In the case of  $6 \text{ keV } D_3^+$  (equaling  $2 \text{ keV/D}$ ),  $600 \text{ eV } D_3^+$  ( $200 \text{ eV/D}$ ) and  $5 \text{ keV } Ar^+$ , flux densities achieved when using the quadrupole doublet lens to focus the beam at the target are also listed

## 5 Summary

SIESTA (Second Ion Experiment for Sputtering and TDS Analysis) is a fully operational setup with a high-current ion source which is suited for well-defined ion-induced erosion and retention studies. It can supply a mass-filtered ion beam of H, D, He or Ar ions with energies of 200 eV – 10 keV with ion flux densities (in the case of 6 keV  $D_3^+ = 2$  keV/D) of up to several  $10^{19}$  atoms  $m^{-2}s^{-1}$  at the target when employing the quadrupole lens to focus the beam, as listed in table 5 for several ion species and energies. Other gas species may potentially be used, but were not tested. Mass filtering is achieved with a dipole magnet capable of deflecting a 10 keV  $Ar^+$  beam. The beam footprint at the target can be modified with the selection of the different beam-defining apertures. The beam footprint measures  $0.5\text{ cm}^2$  in the case of a 6 keV  $D_3^+$  beam at  $0^\circ$  incidence to the target (i.e., normal to the sample surface) with a  $\varnothing$  6 mm beam-defining aperture. The sample may be rotated to study angle-dependent effects and sample temperatures of up to 1300 K are achieved via electron impact heating on the sample backside. The temperature is measured with an infrared pyrometer and a type-K thermocouple. Samples may be inserted into the target chamber with the use of a load-lock. The sample can be weighed in-situ with a magnetic suspension balance located above the target chamber for in-situ weight loss measurements. Thermal desorption spectrometry is available in a dedicated vacuum chamber located below the load-lock for in-vacuo retention studies, though this capability of SIESTA has not yet been tested. The new version of the ion-driven permeation experiment PERMEX [27] is planned for the left exit of the dipole magnet (PERMEX exit in fig. 11).

In this work, the device was assembled and extensively characterized. A parameter scan was performed on the DuoPIGatron ion source, showing an optimal gas flow at which ion currents to the target were maximum. When operating in this regime, the measured ion current at the beam-stopper Faraday cup was proportional to the extraction voltage to the power of  $3/2$  ( $I \propto U^{3/2}$ ), indicating a constant perveance (eq. 2), which would also be the case if the ion source were operating at optimal perveance. Effective mass-filtering was tested for a wide range of ion species and energies. The ion trajectories were simulated with a custom-written code based on the transfer matrix method and the measured beam emittance. Einzel lenses were tested at two positions in the ion optical system, leading in all cases to a strong decrease in the ion current at the target due to loss of space-charge compensation. A quadrupole doublet lens was installed between the dipole magnet and target chamber and is used for simultaneous focusing of the ion beam in the horizontal and vertical plane. If no quadrupole lens is used, the flux density at the target at SIESTA is comparable to that of its predecessor, the HSQ [5]. If the quadrupole lens is employed, the flux density at the target is increased by up to a factor of 4 compared to the HSQ. Table 5 lists deuterium and argon ion flux densities with and without the focusing effect of the quadrupole lens.

The beam footprint at the target was measured with ellipsometry after erosion of 70-nm-thick amorphous hydrogenated carbon films on Si substrates. A homogeneous beam footprint at the target was achieved by sweeping the ion beam over the beam-defining aperture by oscillating the current passing through the dipole magnet. Sample heating was tested on W samples up to 1300 K and a push-rod mechanism was introduced to improve the thermocouple temperature measurement.

The spatially-resolved neutral population within the beam at the position of the target was measured by eroding a 50-nm-thick Au film on a Si substrate and measuring the change of the layer thickness by Rutherford Backscattering Spectrometry (RBS). These experiments resulted in a maximum neutral population of 1.5% and an average population over the measured positions of 0.8%. The magnetic suspension balance was tested by comparing in-situ and ex-situ weight loss measurements of Au samples eroded by a 6 keV  $D_3^+$  beam (2 keV/D), showing a measurement discrepancy of  $20\ \mu\text{g}$  ( $759\ \mu\text{g}$  ex-situ versus  $739\ \mu\text{g}$  in-situ). Additional measures may be required to increase the reliability of the in-situ magnetic suspension balance, such as thermal and electromagnetic shielding. The sputter yield of pure Au under these exposure conditions was determined from the ex-situ and in-situ weight loss measurements. The results agree within 15% with the sputter yield calculated by the sputtering code SDTrimSP [25].

## Acknowledgements

The authors would like to express their gratitude to T. da Silva, A. Manhard, U. von Toussaint, H. Greuner, T. Höschen, J. Roth and M. Reisner for their helpful feedback as well as to A. Friedrich, A. Weghorn, M. Fußeder, J. Dorner and the E2M workshop for their continued support.

## References

- [1] R. Arredondo, M. Oberkofler, K. Schmid, T. Schwarz-Selinger, W. Jacob, and R. Neu. SIESTA: a high current ion source for erosion and retention studies. *Rev. Sci. Instrum.*, 89, 2018.

- [2] J. Roth et al. Recent analysis of key plasma wall interactions issues for ITER. *J. Nucl. Mater.*, 390-391:1–9, 2009.
- [3] R. Behrisch and W. Eckstein. *Sputtering by Particle Bombardment IV*, volume 110 of *Topics in Applied Physics*. Springer Berlin Heidelberg, Berlin, 2007.
- [4] W. Eckstein. Sputtering yields. In R. Behrisch and W. Eckstein, editors, *Sputtering by Particle Bombardment IV*, volume 110 of *Topics in Applied Physics*, chapter Sputtering Yields, pages 33–187. Springer Berlin Heidelberg, Berlin, 2007.
- [5] W. Eckstein, C. Garcia-Rosales, J. Roth, and W. Ottenberger. *Sputtering data*. IPP Report 9/82, Max-Planck-Institut für Plasmaphysik (Ed.) <http://hdl.handle.net/11858/00-001M-0000-0027-6324-6>, 1993.
- [6] R. C. Davis, O. B. Morgan, L. D. Stewart, and W. L. Stirling. A multiampere DuoPIGatron ion source. *Review of Scientific Instruments*, 43(2):278–283, 1972.
- [7] G. Schilling. High power neutral particle beams for fusion research. 5:309–313, 1974.
- [8] C. D. Child. Discharge from hot CaO. *Physical Review (Series I)*, 32(5):492–511, 1911.
- [9] E Speth. Neutral beam heating of fusion plasmas. *Reports on Progress in Physics*, 52(1):57, 1989.
- [10] T. Kalvas. *Development and use of computational tools for modelling negative hydrogen ion source extraction systems*. PhD thesis, University of Jyväskylä, 2013.
- [11] R. Smallwood. *ASTM special technical publication 849: Refractory metals and their industrial applications: a symposium*. ASTM International, 1984.
- [12] F. Paschen. Über die zum funkenübergang in luft, wasserstoff und kohlendioxid bei verschiedenen drucken erforderliche potentialdifferenz. *Ann. Phys.*, 273(5):69–96, 1889.
- [13] H. Liebl. *Applied Charged Particle Optics*. Springer-Verlag Berlin Heidelberg, 1 edition, 2008.
- [14] H. von Koch and L. Friedman. Hydrogen-helium ion-molecule reactions. *The Journal of Chemical Physics*, 38(5):1115–1122, 1963.
- [15] M. Sode. *Quantitative Beschreibung von Wasserstoff-Stickstoff-Argon-Mischplasmen*. PhD thesis, Christian-Albrechts-Universität Kiel, Kiel, 2014.
- [16] J. Grösser. *Einführung in die Teilchenoptik*. B. G. Teubner Stuttgart, 1983.
- [17] L. Seidl. *Optimierung des Ionentransports an der Hochstrom-Ionenquelle HSQ-II*. Bachelor Thesis, Technische Universität München, 2016.
- [18] T. Kalvas. IBSIMU Ion Beam Simulator, 2014.
- [19] N. Chauvin, O. Delferri-Åšre, R. Duperrier, R. Gobin, P. A. P. Nghiem, and D. Uriot. Transport of intense ion beams and space charge compensation issues in low energy beam lines (invited). *Rev. Sci. Instrum.*, 83(2):02B320, 2012.
- [20] M.G. Minty and F. Zimmermann. *Measurement and Control of Charged Particle Beams*. Springer Berlin Heidelberg, 2003.
- [21] J.G. Wang, E. Boggasch, P. Haldemann, D. Kehne, M. Reiser, T. Shea, and D.X. Wang. Performance characteristics of a variable-perveance gridded electron gun. In *IEEE Transaction on Electron Devices*, volume 37, pages 2622–2628. IEEE, 1990.
- [22] J.G. Wang, D.X. Wang, and M. Reiser. Beam emittance measurement by pepper-pot method. *Nucl. Instrum. Methods Phys. Res., Sect. A*, 307:190–194, 1991.
- [23] T. Schwarz-Selinger, A. von Keudell, and W. Jacob. Novel method for absolute quantification of the flux and angular distribution of a radical source for atomic hydrogen. *Journal of Vacuum Science & Technology A: Vacuum, Surfaces, and Films*, 18(3):995–1001, 2000.
- [24] R. Janev, W. Langer, K. Evans, and D. Post. *Elementary Processes in Hydrogen-Helium Plasmas*, volume 4. Springer-Verlag Berlin Heidelberg, 1 edition, 1987.
- [25] A. Mutzke, R. Schneider, W. Eckstein, and R. Dohmen. *SDTrimSP Version 5.00*. IPP Report 12/08, Max-Planck-Institut für Plasmaphysik (Ed.) <http://hdl.handle.net/11858/00-001M-0000-0026-EAF9-A>, 2011.

- [26] H. L. Bay, J. Roth, and J. Bohdanský. Light-ion sputtering yields for molybdenum and gold at low energies. *J. Appl. Phys.*, 48(11):4722–4728, 1977.
- [27] A. V. Golubeva, M. Mayer, Yu. M. Gasparyan, J. Roth, and V. A. Kurnaev. The ion-driven permeation experiment PERMEX. *Review of Scientific Instruments*, 80(7):073501, 2009.